Solvent quality and chromosome folding in *Escherichia coli*

Yingjie Xiang[1,2], Ivan V. Surovtsev[2,3,4], Yunjie Chang[2,5], Sander K. Govers[2,3,4,6], Bradley R. Parry[2,3,4], Jun Liu[2,5], Christine Jacobs-Wagner[2,3,4,5,6,7,*]

[1]Department of Mechanical Engineering and Materials Science, Yale University, New Haven, CT 06520, USA

[2]Microbial Sciences Institute, Yale University, West Haven, CT 06516, USA

[3]Department of Molecular, Cellular, and Developmental Biology, Yale University, New Haven, CT 06520, USA

[4]Howard Hughes Medical Institute, Yale University, New Haven, CT 06520, USA

[5]Department of Microbial Pathogenesis, Yale School of Medicine, New Haven, CT 06510, USA

[6]Department of Biology and ChEM-H Institute, Stanford University, Palo Alto, CA 94305, USA

[7]Lead contact

*Correspondence: jacobs-wagner@stanford.edu

Summary

All cells must fold their genomes, including bacterial cells where the chromosome is compacted into a domain-organized meshwork called nucleoid. Polymer conformation depends highly on the quality of the solvent. Yet, the solvent quality for the DNA polymer inside cells remains unexplored. Here, we developed a method to assess this fundamental physicochemical property in live bacteria. By determining the DNA concentration and apparent average mesh size of the nucleoid, we provide evidence that the cytoplasm is a poor solvent for the chromosome in *Escherichia coli*. Monte Carlo simulations showed that such a poor solvent compacts the chromosome and promotes spontaneous formation of chromosomal domains connected by lower-density DNA regions. Cryo-electron tomography and fluorescence microscopy revealed that the (poly)ribosome density within the nucleoid is spatially heterogenous and correlates negatively with DNA density. These findings have broad implications to our understanding of chromosome folding and intracellular organization.

Keywords

Chromosome folding, nucleoid, solvent quality, chromosome compaction, domain organization, DNA mesh size, ribosome localization

Introduction

All cells, regardless of their origin, must package and organize their genome in a small volume. Proper folding of the chromosomes is critical as it affects many cellular processes, including gene expression, DNA repair and chromosome segregation. Unlike eukaryotic cells, bacterial cells lack a nuclear membrane and do not package their DNA content into repeating structural units akin to nucleosomes. However, they still fold and concentrate their chromosomal material into a dynamic and organized DNA meshwork known as the nucleoid. In many bacterial species, including *Escherichia coli*, the nucleoid does not spread throughout the cell; instead, it is found within a portion of the cytoplasmic space (Figure 1) (Gray et al., 2019; Hobot et al., 1985; Kellenberger et al., 1958; Mason and Powelson, 1956; Piekarski, 1937; Robinow and Kellenberger, 1994). This indicates that the compaction of the bacterial chromosome is not simply dictated by the physical confinement created by the cell envelope. Furthermore, the chromosome displays higher-order organization across multiple length scales (Dame et al., 2020; Verma et al., 2019). For instance, high-resolution chromosome conformation capture (Hi-C) studies in different bacterial species have demonstrated that the chromosome is organized into various "chromosomal interaction domains" (CIDs) within which nearby gene loci interact more frequently with each other than with those outside the domain (Le et al., 2013; Lioy et al., 2018; Marbouty et al., 2014; Marbouty et al., 2015; Val et al., 2016; Wang et al., 2017; Wang et al., 2015).

Apart from its compacted and organized structure, another important, through less appreciated, aspect of the nucleoid is its mesh size (Figure 1), as it impacts the mobility of cytoplasmic components and thereby affects the spatial organization of the cytoplasm. For example, the enrichment of ribosomes/polyribosomes (mRNAs loaded with multiple ribosomes) at the cell poles and in-between segregated nucleoids in *E. coli* and other bacteria is often attributed to nucleoid exclusion (Azam et al., 2000; Bakshi et al., 2012; Gray et al., 2019; Lewis et al., 2000; Robinow and Kellenberger, 1994; Sanamrad et al., 2014). It is, however, difficult to predict which cytoplasmic components are impacted by the nucleoid, as its average mesh size has not been measured in any bacteria.

What are the biophysical principles that help explain the compacted size, domain organization and mesh size of the bacterial nucleoid? Multiple factors are thought to be at play (Surovtsev and Jacobs-Wagner, 2018). They include transcription and other biochemical processes that modulate DNA supercoiling (Dorman, 2019; Ma and Wang, 2016). Bacteria also carry a number of DNA-binding proteins, known as nucleoid-associated proteins (NAPs) and structural maintenance of chromosome

2

66　(SMC) proteins, that alter the structure of the DNA locally or over long molecular distances (Dame et

67　al., 2020; Dillon and Dorman, 2010). While the direct contribution of these proteins to DNA

68　compaction is not entirely clear (Spurio et al., 1992; Wu et al., 2019), NAPs and SMC protein

69　complexes are known to play important roles in the organization and regulation of chromosome

70　architecture at the level of individual genes and CIDs (Dame et al., 2020). In addition, macromolecular

71　crowding is frequently proposed to drive chromosome compaction through steric effects (Cunha et

72　al., 2001; de Vries, 2010; Jeon et al., 2017; Jun, 2015; Odijk, 1998; Pelletier et al., 2012; Shendruk et

73　al., 2015; Wegner et al., 2016; Wu et al., 2019; Yang et al., 2020; Yoshikawa et al., 2010; Zhang et al.,

74　2009; Zimmerman, 1993; Zimmerman and Minton, 1993). The idea is that cytoplasmic components

75　larger than the DNA mesh size (i.e., crowders) will be excluded from the nucleoid, creating an

76　imbalance in component concentration between the nucleoid region and the rest of the cytoplasm.

77　This imbalance results in an effective osmotic pressure that pushes DNA segments closer to each

78　other. The magnitude of compaction driven by this steric repulsion is currently unknown inside cells.

79

80　It is important to note that the DNA and the cytoplasmic components do not interact only sterically,

81　as neither of them are chemically inert. From a simple polymer physics perspective, the cytoplasm

82　can be viewed as a polymer solution: the polymer is the DNA, and the solvent is everything else in the

83　cytoplasm (water, metabolites, proteins, RNAs, etc.) (Figure 1). It is well established that the

84　interaction between a polymer and its solvent directly affects the three-dimensional (3D)

85　conformation of the polymer (Gennes, 1979; Rubinstein, 2003). Based on the polymer-solvent

86　interaction, the quality of a solvent is broadly classified into three types: good, ideal and poor. In a

87　good solvent, interactions between the polymer and the solvent are favored over interactions

88　between polymer segments. Conversely, in a poor solvent, interactions between polymer segments

89　are favored over their interactions with the solvent. When the repulsive and attractive interactions

90　are balanced out (zero net interaction), the solvent is said to be ideal. Despite the well-known

91　importance of the solvent for the polymer conformation, the effects of the solvent quality of the

92　bacterial cytoplasm (or the eukaryotic nucleoplasm) on DNA compaction or organization are unclear.

93　This is presumably because the solvent quality of the cytoplasm (or nucleoplasm) has not been

94　measured and is difficult to predict. Traditional methods for determining the solvent quality of a

95　polymer solution, such as dynamic light scattering, small-angle X-ray scattering, rheology, nuclear

96　and magnetic resonance (Auge et al., 2009; Guettari et al., 2012; Waigh et al., 2001), are unfortunately

97　not suitable for measurements inside cells. In this study, we develop an experimental approach to

98　estimate the solvent quality of the cytoplasm in *E. coli* cells. Our results show that the cytoplasm is a

3

99 poor solvent for the chromosome and that this macroscopic characteristic of the cytoplasm
100 contributes to chromosome folding and intracellular organization.

101

Results

103 As the polymer concentration increases, the polymer solution transitions from the regime of being
104 dilute to semidilute, where the polymer segments overlap to form a meshwork. It is well established
105 in polymer physics that the average mesh size (or correlation length) ξ of a semidilute polymer
106 solution depends not only on properties of the polymer (concentration, rigidity, molecular weight
107 and monomer size), but also on the quality of the solvent (Gennes, 1979; Rubinstein, 2003), as shown
108 in Eq. 1 (see STAR Methods for derivation).

109
$$\xi = \frac{\sqrt{3}}{6} b^{\frac{\nu-1}{3\nu-1}} \left(\frac{18\sqrt{3}M_w}{\pi c N_A l_{bp}} \right)^{\frac{\nu}{3\nu-1}} \tag{1}$$

110 In this equation, the term c represents the average concentration of the polymer. The Flory exponent
111 ν quantifies the solvent quality. It is equal to 0.5 for an ideal solvent, and is smaller than 0.5 for a poor
112 solvent and greater than 0.5 for a good solvent (Rubinstein, 2003). N_A is Avogadro's number. M_w and
113 l_{bp} are the average molecular weight (650 g/mol) and size of a base pair (0.34 nm), respectively
114 (Diekmann et al., 1982; Lee et al., 2012; Peale et al., 1989; Ratilainen et al., 2001; Yonemura and
115 Maeda, 1982). The remaining term, b, is the Kuhn length of the polymer, which is a measure of its
116 rigidity and equals to twice the persistence length of the polymer. DNA is a semiflexible polymer. Its
117 rigidity stems from base stacking interactions within the DNA duplex and electrostatic repulsion
118 among phosphate groups in the DNA backbone. The persistence length of the DNA is often assumed
119 to be 50 nm (i.e., Kuhn length b = 100 nm). However, in vitro measurements of DNA rigidity indicate
120 that the presence of multivalent cations, including Mg^{2+}, the most abundant divalent cation in *E. coli*
121 (Alatossava et al., 1985; Cayley et al., 1991; Kuhn and Kellenberger, 1985; Lusk et al., 1968; Moncany
122 and Kellenberger, 1981), can decrease the DNA persistence length down to 25-35 nm (Baumann et
123 al., 1997; Mantelli et al., 2011; Porschke, 1986; Porschke, 1991). Based on these measurements and
124 the millimolar concentration of Mg^{2+} in the *E. coli* cytoplasm (Alatossava et al., 1985; Cayley et al.,
125 1991; Lusk et al., 1968), the Kuhn length of the chromosomal DNA (b) is estimated to be ~60 nm (i.e.,
126 a persistence length of ~30 nm).

127

128 Given the aforementioned values for b, M_w and l_{bp}, the solvent quality of the cytoplasm can be
129 deduced using Eq. 1 by determining the concentration of the chromosomal DNA within the nucleoid
130 region (c) and the average mesh size of the nucleoid (ξ).

4

131

Average DNA concentration within the nucleoid

133   To determine the average concentration of DNA within the nucleoid, we took advantage that in

134   nutrient-poor environments (e.g., glycerol as a carbon source), *E. coli* cells exhibit discrete B, C and D

135   periods, corresponding to the cell cycle phases before, during and after DNA replication, respectively

136   (Cooper and Helmstetter, 1968). In B-period cells, the DNA mass can be unambiguously determined,

137   as each nucleoid in these cells consists of a single, non-replicating chromosome (Cooper and

138   Helmstetter, 1968). Using a previously described method (Gray et al., 2019), we identified B-period

139   cells within a population by examining cell size and the spatial pattern of the DNA replication marker

140   SeqA fused to mCherry. During DNA replication (C period), SeqA binds the newly synthesized hemi-

141   methylated DNA (Brendler et al., 1995; Lu et al., 1994; Slater et al., 1995; Waldminghaus et al., 2012).

142   This property leads to the formation of fluorescent foci in cells actively replicating DNA (Figure 2A),

143   as shown before (Adiciptaningrum et al., 2015; Gray et al., 2019; Helgesen et al., 2015; Molina and

144   Skarstad, 2004; Wallden et al., 2016). In contrast, SeqA-mCherry displayed a diffuse distribution in

145   cells before and after DNA replication (i.e., during B and D periods, respectively) (Figure 2A). We used

146   these changes in spatial distribution of SeqA-mCherry signal and the knowledge that cells grow in

147   size during the cell cycle to classify cells by cell-cycle period (Figure 2B). Next, we identified the

148   contour of DAPI-stained nucleoids in 19,510 cells in the B period using the objectDetection module

149   of the Oufti software package (Paintdakhi et al., 2016) and quantified their volumes (STAR Methods).

150   We found that nucleoids consisting of one chromosome have an average volume of $\sim$0.7 μm^3 (Figure

151   2C). The mass of the *E. coli* chromosome is about 5×10^{-12} mg given that this chromosome is made of

152     $\sim 4.6 \times 10^6$ base pairs and that the average molecular weight of a base pair is 650 g/mol (Lee et al.,

153   2012; Peale et al., 1989; Ratilainen et al., 2001). From this, we determined the average DNA

154   concentration within the nucleoid region to be 7.1 ± 1.0 mg/ml (Figure 2D). Our measurements,

155   which were done with cells growing at 37°C, were robust to a change in growth temperature to 30°C

156   (Figure S1).

157

158   Under nutrient-rich (fast growth) conditions, *E. coli* cells enlarge to accommodate multi-fork DNA

159   replication. The absence of a discrete B period under these conditions, prevented us from performing

160   the same microscopy analyses as above. However, when we converted bulk measurements of DNA

161   mass per cell made under nutrient-rich growth conditions (Basan et al., 2015) to DNA concentrations

162   within the nucleoid volume (c) by taking into consideration of changes in cell and nucleoid volume,

163   we obtained c = 7.4 ± 0.2 mg/ml (n = 3 nutrient-rich growth conditions, see STAR Methods for

5

164   details). The agreement between this estimation and our single-cell measurements (Figure 2D)

165   indicates that c remains largely constant across nutrient-poor and -rich conditions. This is consistent

166   with both DNA content per cell and nucleoid size scaling with cell size across growth conditions

167   (Basan et al., 2015; Gray et al., 2019; Sharpe et al., 1998).

168

169   Apparent average nucleoid mesh size in *E. coli* cells

170   Given $c \approx 7$ mg/ml, apart from the Flory exponent (ν), the remaining unknown in Eq. 1 is the mesh

171   size (ξ). Studies on biopolymer solutions and hydrogels have demonstrated that particles of size

172   much smaller than the average mesh size diffuse freely through the meshwork (Axpe et al., 2019; Cai

173   et al., 2011; Carn et al., 2012; Wong et al., 2004). When the probe size is close to the average mesh

174   size, the dynamics of the probes becomes impacted by the polymer mesh. This impact exacerbates as

175   the probes increase in size. In the context of the bacterial cell, this implies that probes much smaller

176   than the nucleoid mesh size will diffuse freely in the cytoplasm without any apparent hindrance from

177   the nucleoid (assuming that the particles do not interact with the nucleoid). Such probes will have an

178   equal probability of diffusing inside or outside the nucleoid. In contrast, probes larger than the

179   average mesh size will have a higher probability of diffusing outside the nucleoid, i.e., nucleoid

180   exclusion will increase with increasing probe size.

181

182   If we assume that the cytoplasm is an ideal solvent ($\nu = 0.5$) for the chromosome, the average mesh

183   size should be 22 nm (Eq. 1), in which case particles larger than 22 nm should have their motion and

184   spatial distribution affected by the nucleoid. To test this assumption experimentally, we used an *E.*

185   *coli* strain (CJW6340) that expresses a GFP-tagged, artificially designed protein that self-assembles

186   into a 60-subunit dodecahedron nanocage of 25 nm in diameter (Figure 3A) (Hsia et al., 2016). These

187   nanocages were originally designed for drug and vaccine delivery applications. However, because of

188   their synthetic nature, they are foreign to the bacterial cytoplasm and therefore unlikely to form

189   specific interactions with the nucleoid or other cytoplasmic components, allowing us to repurpose

190   them as intracellular tracers.

191

192   Basal expression of nanocage-GFP proteins (i.e., leaky synthesis) was sufficient to produce a single

193   nanocage-GFP particle per cell in a fraction of the population (Figure 3B). Single-particle tracking

194   experiments revealed no evidence of steric hindrance by the nucleoid, as the nanocage-GFP particle

195   appeared to diffuse freely throughout the cytoplasm (Figure 3C; Video S1). This was further

196   supported by calculating the ensemble-averaged mean squared displacement (MSD) based on all

6

197   particle trajectories measured (n = 85). At the short time scale (first three points), the MSD varied

198   linearly with the time delay, as the slope of MSD curve in the log-log scale was close to 1 (Figure 3D).

199   This indicates that the diffusion of nanocage-GFP particles was Brownian (at the long time scale, the

200   MSD deviated from the linearity due to cell confinement). Furthermore, ensemble calculation of the

201   relative positions of nanocage-GFP particles inside cells demonstrated that the probability density of

202   nanocage-GFP localization is uniform throughout the cytoplasm (n = 2,500 localizations) (Figure 3E).

203   Thus, these 25-nm probes were neither trapped nor excluded by the nucleoid, consistent with their

204   diffusion being Brownian. This result indicates that the nucleoid mesh size is greater than 25 nm,

205   which is inconsistent with the bacterial cytoplasm being an ideal solvent for the chromosome.

206

207   To estimate the average nucleoid mesh size, we used GFP-μNS particles, which are larger probes that

208   our laboratory previously developed to probe the material properties of the cytoplasm (Parry et al.,

209   2014). GFP-μNS is a fluorescent protein fusion to a mammalian reovirus protein that self-assembles

210   into a globular complex (Broering et al., 2005; Broering et al., 2002). Like GFP and the nanocage

211   protein, μNS is not of bacterial origin and is therefore unlikely to display a significant affinity to

212   components of the *E. coli* cytoplasm. When expressed from the chromosome of *E. coli* (CJW4617)

213   following IPTG induction (50-200 μM) for 30 to 120 min (STAR Methods), GFP-μNS assembled into

214   fluorescent particles, usually one per cell (Parry et al., 2014). The size of the GFP-μNS particles, which

215   was deduced by establishing a calibration between the particle sizes and their corresponding

216   fluorescence intensities (Parry et al., 2014) (STAR Methods), ranged from ∼50 to ∼200 nm based on

217   the level of protein expression in each cell (Figure S2).

218

219   We tracked GFP-μNS particles (n = 133,692) and calculated their relative positions in the

220   corresponding cells. We then binned all GFP-μNS particles by size and, for each size bin, constructed

221   a probability density map of the relative particle position in the cells (Figure 3F). These probability

222   density maps indicate the likelihood of finding a GFP-μNS particle at a specific intracellular location

223   across cells. For particles in the bin with the smallest average particle size (51 nm), the probability

224   density map appeared indistinguishable from that obtained for nanocage-GFP particles (Figure 3E),

225   indicating that these particles are not excluded by the nucleoid. This pattern changed in the next size

226   bin, as probes of an average size of 58 nm started to display an increased probability to be localized

227   at the cell pole regions (i.e., away from the nucleoid). This enrichment in probability density of

228   localization at the cell poles continued to increase with probe size (Figure 3F), with ever larger

229   particles becoming less and less likely to be found within the nucleoid region. Particles with the

230   largest average size (150 nm) were almost completely excluded from the nucleoid, as shown by the

231   high probability density of localization at the cell poles and the near-zero probability density

232   elsewhere in the cell. While these ensemble results cannot provide an exact value, they approximate

233   the apparent average nucleoid mesh size to be around 50 nm.

234

235   **The *E. coli* cytoplasm behaves as a poor solvent for the chromosome**

236   Based on $c \approx 7$ mg/ml, $b \approx 60$ nm and $\xi \approx 50$ nm, we found that the corresponding Flory exponent, v,

237   is ~ 0.36 (Eq. 1). Such a small Flory exponent (< 0.5) implies that the bacterial cytoplasm is a poor

238   solvent for the chromosome. Our conclusion is robust against variability in DNA concentration across

239   cells (Figure 2D) or nutrient-poor or -rich growth conditions (see above). For instance, a DNA

240   concentration of 8 mg/ml would correspond to an even smaller Flory exponent (Figure 4A). At DNA

241   concentrations of 6 mg/ml, or even as low as 5 mg/ml, the Flory exponent, v, remains well below 0.5,

242   consistent with the cytoplasm behaving as a poor solvent.

243

244   The phase diagram in Figure 4B shows that our conclusion is also robust to variations in DNA Kuhn

245   length due to potential fluctuations in cytoplasmic ionic strength. To achieve the observed apparent

246   ~ 50-nm nucleoid mesh size in an ideal solvent ($v = 0.5$) or a good solvent (e.g., $v = 0.58$), the Kuhn

247   length of DNA at an average concentration of 7 mg/ml would have to be 26 nm or 13 nm, respectively

248   (Eq. 1). This would mean a DNA persistence length (half the Kuhn length) equal to 13 nm or lower.

249   Such a small value has never been observed experimentally even in solutions of extremely high ionic

250   strength (e.g., 3-4 M NaCl) (Borochov et al., 1981; Kam et al., 1981; Sobel and Harpst, 1991) or in the

251   presence of multivalent ions such as Mg^{2+} (Baumann et al., 1997; Mantelli et al., 2011; Porschke, 1986;

252   Porschke, 1991).

253

254   **A poor solvent promotes the organization of the chromosome into domains**

255   Intriguingly, for a DNA Kuhn length of 60 nm and an average DNA concentration of 7 mg/ml, Eq. 1

256   indicates that the average mesh size decreases as the Flory exponent increases (i.e., as the solvent

257   quality improves) (Figure 4A). To understand how the solvent quality of the cytoplasm affects the

258   nucleoid mesh size at the given DNA concentration and Kuhn length, we performed 3D Monte Carlo

259   simulations of chromosome conformation in poor ($v = 0.36$), ideal ($v = 0.50$) and good ($v = 0.58$)

260   solvents (STAR Methods). For all simulations, we modeled the entire *E. coli* chromosome (4.6 million

261   base pairs, contour length ≈ 1.6 mm) as a chain of 26,066 segments, with each segment having a

262   length of 60 nm (corresponding to the Kuhn length). To achieve the average DNA concentration

8

263   observed in actual nucleoids (7 mg/ml), we confined the entire chromosome within a

264   spherocylindrical space with a volume (0.70 μm³) equal to the experimentally determined average

265   nucleoid volume in B-period cells (Figure 2C).

266

267   The simulations revealed a drastic difference in chromosomal conformation when varying the

268   solvent quality (Video S2). The DNA density in the poor solvent appeared to be much more spatially

269   heterogeneous than that in the ideal or good solvent. This was also evident in cross-sectional slices

270   of simulated chromosomes in which each dot represents a DNA segment crossing the plane (Figure

271   5A). The spatial heterogeneity of DNA density in the poor solvent condition compared to the other

272   conditions was also apparent in the two-dimensional (2D) histograms showing the probability

273   density of finding a DNA segment inside subregions of the nucleoid (Figure 5B). This result is

274   consistent with the spatial heterogeneity of DNA density observed in super-resolution fluorescence

275   images of bacterial nucleoids (Le Gall et al., 2016; Marbouty et al., 2015; Spahn et al., 2014; Spahn et

276   al., 2018; Stracy et al., 2015).

277

278   In the poor solvent simulations, DNA segments were locally attracted to each other, leading to the

279   formation of regions with high DNA density interspersed with regions of low DNA density. This

280   spatial heterogeneity in DNA density created "holes" (Figure 5A; Video S2), which may increase the

281   apparent average mesh size and allow larger objects to pass through the nucleoid. Meanwhile, the

282   DNA density of the nucleoid was more spatially homogenous in the ideal and good solvents (Figure

283   5A; Video S2), likely contributing to the smaller apparent average mesh size.

284

285   The denser, domain-like regions of the nucleoid in the poor solvent (Figure 5A-B; Video S2) reminded

286   us of CIDs reported in Hi-C studies in *E. coli* and other bacteria (Le et al., 2013; Lioy et al., 2018;

287   Marbouty et al., 2014; Marbouty et al., 2015; Val et al., 2016; Wang et al., 2017; Wang et al., 2015). To

288   examine this more closely, we calculated the Euclidean distance between pairs of DNA loci along

289   simulated chromosomes binned by 10-kilobase pairs. From this information, we created average

290   maps that indicate the distances between the pairs of DNA loci along the entire simulated

291   chromosomes or a 500-kb region under a poor, ideal or good solvent condition (Figure 5C-D). Along

292   the diagonal of the distance maps, the distance is always 0 (black), because the separation between

293   any given DNA locus and itself is zero by definition. Dark patches along the diagonal in the distance

294   maps represent individual domain-like structures, in which DNA loci that extend a relatively large

295   genomic distance remain in close spatial proximity to each other. Large domain-like structures were

9

296   only seen under the poor solvent condition (Figure 5C-D). Thus, by itself, the poor solvent quality of

297   the cytoplasm results in the formation of chromosomal domains that are reminiscent of CIDs seen in

298   Hi-C experiments.

299

300   However, the poor solvent quality of the cytoplasm alone cannot explain *where* these domains form.

301   In our simulations, the DNA has no sequence information. Therefore, the formation of domains can

302   occur anywhere along the DNA polymer, as shown by randomly averaging 10 different simulated

303   chromosomes (Figure S3A). In Hi-C experiments, results are based on the average of billions of cells.

304   In our case, averaging more simulated chromosomes (e.g., 100) resulted in the disappearance of

305   distinct domain boundaries in distance maps (Figure 5E and Figure S3B). Interestingly, Hi-C

306   experiments on rifampicin-treated *Caulobacter crescentus* cells show that global inhibition of

307   transcription results in the dissolution of most domain boundaries (Le et al., 2013). Collectively, our

308   results suggest that the poor solvent quality of the cytoplasm promotes domain formation, but DNA

309   sequence-dependent factors (e.g., transcription) are responsible for setting the domain boundaries

310   at consistent chromosomal locations across cells (see Discussion).

311

312   Spatial heterogeneity in ribosome density within the nucleoid correlates negatively

313   with DNA density

314   With the poor solvent quality of the cytoplasm resulting in spatial heterogeneity of DNA density, we

315   reasoned that this may, in turn, affect the spatial distribution of other cytoplasmic components, even

316   within the nucleoid region. Specifically, we hypothesized that ribosomes (which exist mostly in

317   polyribosome form) are not only enriched outside of the nucleoid region (Azam et al., 2000; Bakshi

318   et al., 2012; Gray et al., 2019; Robinow and Kellenberger, 1994; Sanamrad et al., 2014), but also

319   heterogeneously distributed throughout the nucleoid due to its uneven DNA density. To test this

320   hypothesis, we prepared frozen-hydrated cryo-electron tomography (cryo-ET) samples of

321   exponentially growing *E. coli* cells (MG1655) (Figure 6A, STAR Methods). To visualize the native *E.*

322   *coli* cytoplasm with higher contrast and resolution, we used cryo-focused ion beam (cryo-FIB) milling

323   to produce lamellae of a thickness between 150 and 260 nm (Figure 6A and Figure S4A-B). Lamella

324   reconstruction revealed ribosomes as dark spots distributed within the *E. coli* cytoplasm (Figure 6B;

325   Video S3).

326

327   To precisely localize the ribosomes, we used the template search routines in emClarity (Himes and

328   Zhang, 2018) to obtain 3D positions and orientations of the ribosomes detected in the lamella

10

329 tomograms. Sub-volumes of the detected ribosomes were aligned and classified (STAR Methods,
330 Figure S4C-D) (Winkler, 2007; Winkler et al., 2009). The average ribosome structure calculated using
331 the detected ribosomes was similar to that of the low-pass filtered reference structure (Figure 6C;
332 Video S4) (Fu et al., 2019), suggesting a high degree of accuracy in our detection procedure. In total,
333 we detected 5,028 ribosomes in the tomogram represented in Figure 6D. Based on the volume of the
334 lamella (0.21 μm^3), the average ribosome density in the tomogram was approximately 24,000 μm^{-3},
335 which is consistent with the reported ribosome density under similar growth conditions (Bakshi et
336 al., 2012; Bremer and Dennis, 2008). We found that the density of (poly)ribosomes was highly
337 heterogeneous across the lamella. This was readily apparent after the Gaussian smoothing of the
338 ribosome density map (Figure 6E and Figure S4E). In addition to the expected accumulation of
339 (poly)ribosomes at the cell periphery (i.e., away from the nucleoid region), (poly)ribosomes
340 displayed heterogeneity in density across the cytoplasm, including within the expected nucleoid
341 region (i.e., central region of the cell).

342

343 Since DNA cannot be directly visualized in the tomograms, we turned to fluorescence microscopy to
344 examine whether the spatial heterogeneity in ribosome density within the nucleoid region is linked
345 to differences in DNA densities. We imaged DAPI-stained *E. coli* cells (CJW7020) producing 50S
346 ribosomal protein L1 tagged with monomeric superfolder GFP (Figure 7A-B). As before, in each cell
347 (*n* = 1,126), we identified the nucleoid outlines based on the DAPI signal (dotted lines in Figures 7A-
348 B). When calculating the correlation between the DNA and ribosome fluorescence signals, we
349 considered only image pixels well within the nucleoid region—at least two pixels away from the
350 nucleoid outline (third row images in Figure 7A-B)— to prevent any bias in the correlation analysis
351 due to the well-known enrichment of (poly)ribosomes outside the nucleoid region. We then
352 calculated the correlation coefficient (Spearman's ρ) between the fluorescence signals of DAPI (DNA)
353 and L1-msfGFP (ribosome) at the single-pixel resolution. We found that even well within the
354 nucleoid, the ribosome fluorescence signal correlates negatively with the DNA signal, as shown with
355 two cell examples (Figure 7C-D) as well as at the population level (*n* = 1,126 cells, Figure 7E). These
356 findings are consistent with the idea that the solvent quality of the cytoplasm contributes to the
357 uneven DNA density, which, in turn, affects (poly)ribosome localization (or vice versa, see
358 Discussion).

359

360

11

361 **The poor solvent quality of the cytoplasm contributes to significant chromosome**
362 **compaction**

363 In addition to the internal mesh size and domain organization, compaction is another biophysical
364 characteristic associated with the bacterial chromosome. A polymer is intrinsically more compact in
365 a poor solvent because polymer segments preferentially interact with themselves rather than with
366 the solvent. This fact prompted us to examine the level of compaction that the poor solvent quality of
367 the cytoplasm could impose on the nucleoid. In our previous Monte Carlo simulations, the
368 chromosome was modeled within the experimentally determined average volume of the nucleoid
369 region (0.7 μm³) to keep the DNA concentration constant (i.e., 7 mg/ml) across solvent types. We
370 performed another set of Monte Carlo simulations, but this time in an unbounded space to examine
371 how the quality of the solvent affects the compaction of the chromosome (STAR Methods). The
372 simulation results showed that the chromosome is most compact in the poor solvent condition, while
373 being the most expanded in the good solvent (Video S5). The ideal solvent was associated with an
374 intermediate phenotype.

375

376 To quantify the size of each simulated chromosome, we calculated its radius of gyration (STAR
377 Methods). In these calculations, we took into consideration the circular geometry of the bacterial
378 chromosome. Given a fixed contour length, the geometric constraint of being circular forces the
379 chromosome to adopt a smaller average size compared to that of a linear chain. Quantitatively, the
380 average radius of gyration of a circular polymer is a factor of $\sqrt{2}$ smaller than that of its linear
381 counterpart (Casassa, 1965; Kramers, 1946; Rubinstein, 2003; Zimm and Stockmayer, 1949). We
382 found that the volume of a circular DNA polymer of the same contour length as the *E. coli*
383 chromosome is, on average, ~9 μm³ in a poor solvent (v = 0.36) compared to ~100 μm³ in an ideal
384 solvent (v = 0.50) or ~550 μm³ in a good solvent (v = 0.58) (Figure 8). Thus, the poor solvent quality
385 of the cytoplasm results in an additional ~10- and ~60-fold chromosome compaction, compared to
386 the ideal and good solvent, respectively. This result suggests that the poor solvent quality of the
387 cytoplasm plays a large role in chromosome compaction.

388

389 We note that this solvent effect alone cannot explain the full compaction of a single chromosome
390 inside cells, as the actual volume of the nucleoid in B-period *E. coli* cells (Figure 2C) is still around 10
391 times smaller (Figure 8, inset). This is consistent with other compacting factors (e.g., DNA
392 supercoiling, NAPs and macromolecular crowding) playing important roles as well (see Discussion).

393

12

Discussion

394

395   The conformation of a given polymer depends on the quality of its solvent (Gennes, 1979; Rubinstein,

396   2003), yet, the solvent quality of the cellular milieu for the chromosome has been long overlooked,

397   most likely due to the lack of a suitable method for its measurement inside cells. In this study, we

398   developed such a method by taking a simple polymer physics perspective of the bacterial cytoplasm

399   as a semidilute polymer solution, in which the chromosome is the polymer and its solvent is

400   comprised of everything else in the cytoplasm. Using this approach, we found that the *E. coli*

401   cytoplasm is a poor solvent for the chromosome and that this physicochemical property inherently

402   interconnects three different aspects of the chromosome inside cells: compaction, mesh size and

403   domain organization.

404

Chromosome compaction

406   A significant level of compaction has long been considered mandatory for the bacterial chromosome

407   to fit inside the cell. This was first suggested by early electron microscopy studies, where the

408   chromosomes released from lysed cells were found to enlarge many times over the size of the cell

409   (Kavenoff and Bowen, 1976; Kavenoff and Ryder, 1976). Dilution of NAPs and loss of macromolecular

410   crowding are likely to contribute to this large nucleoid expansion, as often proposed. However, the

411   solvent for the chromosome also drastically changed in these experiments, from the cytosol—a

412   complex mixture of cytoplasmic components—to a simpler aqueous solution mostly composed of

413   buffering reagents. Any considerable change in the chemical nature of a solvent is expected to affect

414   the solvation and conformation of a dissolved polymer. In light of our finding that the cytoplasm

415   behaves as a poor solvent for the chromosome, it is likely that the swelling of the chromosome

416   following cell lysis is, at least in part, due to the release of the chromosome into a better solvent. Our

417   work shows that in the cytoplasm, the chromosome is more likely to interact with itself compared to

418   the rest of the cytoplasm. In such a poor solvent, preferential interaction (i.e., attraction) between

419   parts of the chromosome compacts the entire chromosome ~10 to ~60 times more than if it were

420   dissolved in an ideal or good solvent, respectively (Figure 8; Video S5).

421

422   Our finding also provided an opportunity for us to more carefully estimate how much a polymer of

423   the contour length of the *E. coli* chromosome would need to be compacted to fit into the nucleoid

424   region of an *E. coli* cell. Previous back-of-the-envelope calculations by different groups (Bloomfield,

425   1997; Holmes and Cozzarelli, 2000; Joyeux, 2014; Jun, 2015; Trun and Marko, 1998; Verma et al.,

426   2019), including ours (Surovtsev and Jacobs-Wagner, 2018), suggested a compaction on the order of

13

427 1000-fold. These estimations relied on three assumptions. (i) Without prior knowledge, the bacterial

428 cytoplasm was assumed to be an ideal solvent for the chromosome. As such, the chromosome was

429 treated as an *ideal* chain that assumes the conformation of a random walk. In other words, the net

430 interaction between the chromosome and the rest of the cytoplasm was assumed to be zero. (ii) The

431 DNA Kuhn length was assumed to be 100 nm (i.e., persistence length = 50 nm). This is a popular

432 assumption, but in the context of the cell, it neglects the impact of the high ionic strength and

433 presence of multivalent ions in the cytoplasm. Indeed, an underappreciated result in the

434 aforementioned electron microscopy studies was the observation that expansion of the released

435 chromosomes after cell lysis was considerably reduced with increasing salt concentrations (Kavenoff

436 and Bowen, 1976). Furthermore, the phase diagram in Figure 4B shows that for a Kuhn length of 100

437 nm (persistence length = 50 nm), the average mesh size would be 13 nm. Such a small average mesh

438 size is incompatible with our findings (Figure 3) or the well-known coupling between transcription

439 and translation in bacteria, which requires ribosomal subunits (~25 nm) to penetrate the nucleoid

440 (see below). (iii) The chromosome was assumed to be linear, neglecting the small relative decrease

441 in polymer size expected after adjusting for its circularity (Casassa, 1965; Kramers, 1946; Rubinstein,

442 2003; Zimm and Stockmayer, 1949).

443

444 After accounting for the solvent quality of the cytoplasm, the estimated rigidity of the DNA under

445 physiological conditions and the circularity of the chromosome (STAR Methods), we found that the

446 theoretical estimation of the chromosome goes down to ~9 μm^3, which is only ~10-fold (as opposed

447 to 1,000-fold) larger than its experimentally determined size in cells (Figure 8, inset). The remaining

448 compaction needed is likely achieved by other compacting factors such as DNA supercoiling, NAPs,

449 nucleoid-associated RNAs and macromolecular crowding (Cunha et al., 2001; Dame, 2005; de Vries,

450 2010; Hammel et al., 2016; Jeon et al., 2017; Jun, 2015; Macvanin et al., 2012; Odijk, 1998; Pelletier

451 et al., 2012; Qian et al., 2017; Shendruk et al., 2015; Wegner et al., 2016; Wu et al., 2019; Yang et al.,

452 2020; Yoshikawa et al., 2010; Zhang et al., 2009; Zimmerman, 1993; Zimmerman and Minton, 1993),

453 though some of these factors may also contribute to the poor solvent quality of the cytoplasm (see

454 below).

455

456 **Nucleoid mesh size**

457 The membrane-less nucleoid not only stores genetic information but also functions as a mesh-like

458 physical barrier that can affect the diffusion and spatial distribution of cytoplasmic components.

459 Therefore, the mesh size of the nucleoid is an important length scale to consider. By assessing the

14

460   degree of nucleoid exclusion for fluorescent probes of varying sizes (25-150 nm), we estimate the

461   apparent average nucleoid mesh size to be around 50 nm in exponentially growing *E. coli* cells (Figure

462   3). This length scale has several physiological implications. For instance, it allows cytoplasmic

463   components of sizes well below 50 nm (e.g., metabolites, proteins, most protein complexes) to diffuse

464   unimpededly in the presence of the nucleoid. As a result, most of the cytoplasm is "well mixed",

465   facilitating biochemical processes. Since the sizes of free ribosomal subunits are ~23 to 26 nm

466   (Boublik, 1985; Verschoor et al., 1985; Zhu et al., 1997), the 50-nm exclusion size of the nucleoid also

467   enables the coupling between transcription and translation by allowing free ribosomal subunits to

468   reach nascent mRNAs within the nucleoid through diffusion (Sanamrad et al., 2014). If the cytoplasm

469   was an ideal or good solvent, our work suggests that the observed high concentration of the DNA (7

470   mg/ml) within the nucleoid region would lead to an average mesh size of 20 nm or smaller (Figure

471   4B) due to the relatively high overlapping of DNA segments with each other (Figure 5A; Video S2).

472   Such a small average mesh size would, at least partly, exclude ribosomes and their subunits from the

473   nucleoid, hindering co-transcriptional translation. Under this scenario, translation would have to

474   primarily take place after transcription has completed and bare (ribosome-free) mRNAs have

475   diffused out of the nucleoid. Such a decoupling between transcription and translation would not only

476   lead to a delay in protein synthesis, but may also shorten the lifetime of mRNAs, as ribosome binding

477   reduces mRNA degradation (Deana and Belasco, 2005; Dreyfus, 2009).

478

479   Our data predict that the diffusion and spatial distribution of cytoplasmic components larger than 50

480   nm are impacted by the presence of the nucleoid in the cytoplasm. We expect that some (possibly

481   most) polyribosome species belong to this category. This reasoning is consistent with the

482   observation that ribosomes, which are mostly found as polyribosomes (Dai et al., 2016;

483   Forchhammer and Lindahl, 1971; Phillips et al., 1969; Varricchio and Monier, 1971), display

484   timescale-dependent sub-diffusive dynamics (Gray et al., 2019), as we may expect for objects that

485   experience caging and uncaging events (Brangwynne et al., 2009; Cai et al., 2011; Guo et al., 2014;

486   Tseng et al. 2004; Wong et al., 2004). Furthermore, other experiments suggest that gene loci and

487   active RNA polymerases (and associated nascent mRNAs) preferentially relocate to the nucleoid

488   periphery during transcription and translation (Cabrera and Jin, 2003; Libby et al., 2012; Stracy et

489   al., 2015; Yang et al., 2019). Once polyribosomes escape the nucleoid, they are less likely to get back

490   inside the nucleoid due to their large size. As a consequence, nucleoid exclusion of polyribosomes

491   leads to ribosome enrichment outside the nucleoid (Azam et al., 2000; Bakshi et al., 2012; Gray et al.,

492   2019; Robinow and Kellenberger, 1994; Sanamrad et al., 2014). The spatial heterogeneity of the DNA

15

493   density across the nucleoid implies that some regions of the nucleoid are more compacted than

494   others. This is consistent with the spatial heterogeneity of (poly)ribosomes seen by cryo-electron

495   tomography (Figure 6 and Figure S4) and fluorescence microscopy (Figure 7). We expect that the

496   motion and spatial distribution of other large (>50 nm) cellular components, such as storage

497   granules, plasmids, bacterial microcompartments (protein-based metabolic organelles) and stress-

498   induced protein aggregates, are also impacted by the nucleoid, for which there is some evidence

499   (Chowdhury et al., 2014; Henry and Crosson, 2013; Racki et al., 2017; Reyes-Lamothe et al., 2014;

500   Wang et al., 2016; Winkler et al., 2010).

501

Chromosome domain organization

503   The bacterial chromosome is not simply stuffed into the cell; it is instead organized over several

504   length scales (Dame et al., 2020; Verma et al., 2019). Notably, recent Hi-C experiments have shown

505   that the chromosome is partitioned into various domains (CIDs) in which DNA loci preferentially

506   interact with each other (Le et al., 2013; Lioy et al., 2018; Marbouty et al., 2014; Marbouty et al., 2015;

507   Val et al., 2016; Wang et al., 2017; Wang et al., 2015). How these domains form is not fully understood.

508   Our Monte Carlo simulations show that at the physiological DNA concentration of 7 mg/ml, a poor

509   solvent leads to high spatial heterogeneity in DNA density within the nucleoid (Figure 5A-B; Video

510   S2), which is consistent with 3D super-resolution fluorescence microscopy observations of

511   fluorescently-labeled nucleoids in *E. coli* (Le Gall et al., 2016; Marbouty et al., 2015; Spahn et al., 2014;

512   Spahn et al., 2018; Stracy et al., 2015). Such spatial heterogeneity is a consequence of the formation

513   of much less dense DNA regions. By calculating the distance between pairs of DNA segments, we

514   found that the dense regions of the simulated chromosomes correspond to neighboring segments

515   that are spatially clustered together (Figure 5C-D), forming domain-like structures of resemblance to

516   CIDs in Hi-C experiments. In contrast, the simulated chromosomes in an ideal or good solvent were

517   much more homogenous in DNA density (Figure 5B), showing very few, if any, domains of significant

518   size (Figure 5C-D). This argues that the poor solvent quality of the cytoplasm promotes the

519   spontaneous formation of chromosomal domains. There is a precedent for such a solvent-driven

520   structural organization of a biopolymer, as protein folding is highly dependent on the poor solvent

521   condition in vitro (Haran, 2012).

522

523   In our simulated chromosomes, domain boundaries were able to form at any chromosomal position

524   (Figure S3A). As a result of this stochasticity, boundaries between domains became increasingly less

525   defined as more distance maps of simulated chromosomes were averaged (Figure 5E and Figure

526 S3B). This is in contrast with Hi-C contact maps in which boundaries of CIDs remain visible despite
527 averaging over billions of cells. Our data therefore suggest that the poor solvent quality of the
528 cytoplasm promotes domain organization of the chromosome, but the specific positions of the
529 domain boundaries seen in Hi-C maps must be attributed to other factors. Indeed, high
530 transcriptional activity is an important determinant of CID boundaries (Le et al., 2013; Le and Laub,
531 2016; Lioy et al., 2018; Marbouty et al., 2015). In our simulated chromosomes, the domains and their
532 boundaries correspond to DNA regions of high and low densities, respectively. This also appears to
533 be true inside cells, as DNA at the CID boundaries is less condensed (more extensible) than the DNA
534 within CIDs (Le and Laub, 2016). Besides gene expression, other factors, such as NAP binding and
535 membrane attachment, may also contribute to the predominance of specific domain boundaries
536 across cells (Lioy et al., 2018; Marbouty et al., 2014).

537

538 Our observation that distinct domain boundaries vanished upon averaging a large number of
539 simulated chromosomes (Figure 5E and Figure S3B) highlights how variability in domain
540 organization may be missed in Hi-C experiments performed on cell populations. At the single-cell
541 level, the structure of the actual chromosome (e.g., size and position of the domains and their
542 boundaries) may considerably differ across cells or change over time, which would be obscured after
543 averaging all identified contacts between DNA loci across a cell population. Consistent with this idea,
544 single-cell Hi-C experiments in eukaryotes have shown that chromosome folding is highly
545 heterogeneous across cells, with the positions of contact enrichments being highly variable (Flyamer
546 et al., 2017; Nagano et al., 2013; Nagano et al., 2017; Ramani et al., 2017; Stevens et al., 2017; Tan et
547 al., 2018; Tan et al., 2019). It would be interesting to perform similar single-cell Hi-C experiments in
548 bacteria. Based on our results, we envision that the solvent quality of the cytoplasm may contribute
549 to some stochasticity in chromosome conformation.

550

551 **What may contribute to the poor solvent quality of the cytoplasm?**
552 There are many ways a solution can be a poor solvent for a given polymer. A poor solvent is a solution
553 in which the net interaction between the polymer and the solvent is energetically unfavorable
554 regardless of the nature of such interactions (e.g., electrostatic, hydrophobic, van der Waals, or
555 hydrogen bonding). Due to the complex chemical composition of the bacterial cytoplasm, the
556 observed poor solvent quality of the cytoplasm is unlikely to originate from a single mechanism. A
557 combination of factors is expected to be in action.

558

17

559 Among these factors, NAPs are attractive candidates. Due to their high abundance and specific
560 interactions with the chromosome, the contribution of NAPs to the poor solvent quality of the
561 cytoplasm may be direct or indirect. In vitro, NAPs have been shown to bend, loop, wrap or bridge
562 DNA segments (Dame et al., 2020; Dillon and Dorman, 2010). These molecular interactions may
563 promote local attraction among nearby chromosomal segments in vivo. In addition, we speculate that
564 NAPs, and potentially other DNA-binding proteins (such as transcriptional regulators), may act as an
565 interface that indirectly modulates the chemical interaction between the chromosome and other
566 cellular components of the cytoplasm. Protein binding to the anionic DNA polymer could, for
567 instance, locally alter the electrostatic potential of the chromosome.

568

569 There are several lines of evidence suggesting that RNAs may also contribute to the poor solvent
570 quality of the cytoplasm for the DNA. (i) Rifampicin treatment of *E. coli*, which blocks transcription
571 initiation and leads to mRNA depletion through degradation (Bernstein et al., 2002; Chen et al., 2015;
572 Selinger et al., 2003), results in nucleoid expansion (Bakshi et al., 2014; Bakshi et al., 2012; Cabrera
573 et al., 2009; Cabrera and Jin, 2003; Dworsky and Schaechter, 1973; Pettijohn and Hecht, 1974; Sun
574 and Margolin, 2004). Conversely, chloramphenicol treatment, which stabilizes mRNAs (Lopez et al.,
575 1998; Pato et al., 1973; Schneider et al., 1978), is associated with nucleoid compaction (Bakshi et al.,
576 2014; Bakshi et al., 2012; Cabrera et al., 2009; van Helvoort et al., 1996; Zimmerman, 2002). These
577 observations are often interpreted as a consequence of a loss or gain of polyribosome crowding in
578 rifampicin- or chloramphenicol-treated cells, respectively. The idea is that polyribosomes create a
579 depletion force through a volume exclusion effect. However, a mutually non-exclusive alternative is
580 that the chemical nature of these mRNAs, and not just the size of the polyribosomes, plays a role by
581 affecting the quality of the solvent for the chromosome. (ii) The spatial organization of gene
582 expression in *E. coli* is also consistent with RNAs contributing to the poor solvent quality of the
583 cytoplasm. As mentioned above, although transcription can start within the nucleoid, gene loci have
584 been shown to relocate to the nucleoid periphery during transcription (Libby et al., 2012; Yang et al.,
585 2019). This is consistent with the accumulation of active RNA polymerases at the periphery of the
586 nucleoid and regions of low DNA densities (Stracy et al., 2015). This has led to a model in which
587 actively transcribed gene loci with their associated RNA polymerases and nascent mRNAs segregate
588 away from the nucleoid bulk. Importantly, gene relocation occurs independently of concurrent
589 translation, i.e., without the loading of the bulky ribosomes (Yang et al., 2019). These observations
590 support the idea that the interaction between mRNA and DNA is unfavorable (i.e., repulsive). (iii)
591 Repulsive interaction between mRNA and DNA is also consistent with the finding that high levels of

18

592   long transcripts drive the local establishment of chromosomal domain boundaries (Le et al., 2013; Le
593   and Laub, 2016; Lioy et al., 2018; Marbouty et al., 2015). At the domain boundary, high
594   transcriptional activity leads to an accumulation of nascent mRNAs. Since these mRNAs are still
595   bound to the DNA through the RNA polymerases, they cannot diffuse away. We envision that in order
596   to minimize the contact with these bound mRNAs, nearby DNA strands retract to the flanking sides,
597   reducing their local density at the boundary while forming denser DNA regions (domains) on both
598   sides of the boundary. Such a DNA retraction would be mainly driven by its unfavorable interaction
599   with the mRNA and not by the steric blocking of ribosomes, as the formation of a domain boundary
600   occurs in the absence of translation (Le and Laub, 2016).

601

602   Another potential contributing factor to the poor solvent quality of the cytoplasm is its high ionic
603   strength (Alatossava et al., 1985; Cayley et al., 1991; Kuhn and Kellenberger, 1985; Lusk et al., 1968;
604   Moncany and Kellenberger, 1981; Roe et al., 1998; Schultz et al., 1962). In vitro studies have shown
605   that the net interaction between DNA fragments becomes more attractive with increasing salt
606   concentrations (Nicolai and Mandel, 1989). Divalent Mg^{2+}, but not monovalent Na^+, has been found
607   to not only screen the charges on DNA but also induce attraction among the strands (Qiu et al., 2007).
608   Overall, the poor solvent quality is likely to originate from interspersed and superimposed molecular
609   interactions associated with the complex chemical nature of the bacterial cytoplasm.

610

Acknowledgements

617

Author Contributions

619   Conceptualization, Y.X. and C.J.-W.; Methodology, Y.X., I.V.S., Y.C., S.K.G., B.R.P. and C.J.-W. Software,
620   Y.X.; Formal Analysis, Y.X., I.V.S., Y.C. and B.R.P.; Investigation, Y.X., I.V.S., Y.C., S.K.G. and B.R.P.; Data
621   Curation, Y.X., I.V.S., Y.C., S.K.G. and B.R.P.; Writing – Original Draft, Y.X. and C.J.-W.; Writing – Review
622   & Editing, Y.X., I.V.S., Y.C., S.K.G., B.R.P., J.L. and C.J.-W; Visualization, Y.X., I.V.S., Y.C. and C.J.-W.;
623   Supervision, J.L and C.J.-W.; Project Administration, C.J.-W.; Funding Acquisition, C.J.-W.

624

19

Declaration of Interests

626 The authors declare no competing interests.

627

Figure legends

629 **Figure 1. The *E. coli* cytoplasm viewed from a polymer physics perspective.**

630 Schematic showing the *E. coli* chromosome folded into a meshwork structure known as the nucleoid.
631 The nucleoid mesh size is denoted as ξ. The cytoplasm can be viewed as a semidilute polymer
632 solution, where the DNA is the polymer and the rest of the cytoplasm acts as its solvent.

633

634 **Figure 2. Estimation of the average DNA concentration in the nucleoid region in B-period *E.***
635 ***coli* cells.**

636 A. Fluorescence images of representative DAPI-stained CJW6324 cells in different cell cycle periods:
637 B, C and D periods (i.e., before, during and after the DNA replication). The green and yellow outlines
638 are the cell and nucleoid contours detected by the software package Oufti.

639 B. Plot showing the relative area of the SeqA-mCherry signal as a function of cell area. The contour
640 lines (from light to dark color) represent the 25%, 50% and 75% probability envelopes of the data.

641 C. Probability density function of the estimated nucleoid volume in B-period cells.

642 D. Probability density function of the average DNA concentration calculated based on the total mass
643 of the *E. coli* chromosome and the nucleoid volume measurements shown in panel C.

644 See also Figure S1.

645

646 **Figure 3. Estimation of the average nucleoid mesh size.**

647 A. Schematic of an assembled nanocage-GFP particle. The particle has a dodecahedron shape (Hsia et
648 al., 2016).

649 B. Fluorescence images of nanocage-GFP particles assembled in *E. coli* cells (CJW6340).

650 C. Example of nanocage-GFP particle trajectory. The gray outline indicates the cell contour detected
651 by the Oufti software package using the corresponding phase image of the cell.

652 D. Log-log ensemble-averaged mean squared displacement (MSD) based on individual trajectories of
653 nanocage-GFP particles (n = 85). The slope (α = 0.97) was fitted based on the first three time delays.

654 E. Probability density map of the localization of nanocage-GFP particles. The density map was
655 constructed by plotting the normalized 2D histogram of the relative particle positions.

656 F. Probability density maps of the localization of GFP-µNS particles as a function of their size. The
657 positions of the particles (n = 133,692) were determined relative to the cell contours. Particles were

20

658　then binned by their sizes, as indicated. For each particle-size bin, a probability density map of

659　particle localizations was constructed, as described in panel E.

660　See also Figure S2 and Video S1.

661

662　**Figure 4. Relationship between solvent quality, polymer concentration, Kuhn length and mesh**

663　**size**.

664　A. Plot showing the average mesh size of the nucleoid as a function of the Flory exponent, with a DNA

665　Kuhn length of 60 nm and various DNA concentrations (5, 6, 7 or 8 mg/ml) calculated using Eq. 1.

666　B. Heatmap showing the average nucleoid mesh size calculated using Eq. 1 with different

667　combinations of DNA Kuhn lengths and Flory exponents, at a given DNA concentration of 7 mg/ml.

668

669　**Figure 5. Monte Carlo simulations of the *E. coli* chromosome conformation in different types**

670　**of solvent.**

671　The entire *E. coli* chromosome was modeled using Monte Carlo simulations (STAR Methods).

672　Chromosomes were simulated within the confinement of a spherocylinder with a volume equal to

673　that of an average nucleoid ($\sim$0.7 μm^3) in a poor (v = 0.36), ideal (v = 0.50) and good solvent (v =

674　0.58). The Kuhn length of the DNA was assumed to be 60 nm.

675　A. Example slices of simulated chromosomes in a poor, ideal or good solvent. Each dot represents a

676　DNA segment going in or out of the slices (XY- or YZ- plane).

677　B. Density maps of the slices shown in panel A. The maps were constructed as the normalized 2D

678　histograms of positions of the simulated DNA segments.

679　C. Distance maps indicating the spatial separation between any two loci along the simulated

680　chromosomes in the poor, ideal or good solvent. Each map is a result of averaging 10 simulated

681　chromosomes.

682　D. Distance maps as in panel C, except for showing only the first 500-kb region of the simulated

683　chromosomes.

684　E. Distance maps as in panel D, except that 100 simulated chromosomes were averaged instead of 10.

685　See also Figure S3 and Video S2.

686

687　**Figure 6. Spatial distribution of ribosomes in *E. coli* tomograms.**

688　A. Schematic showing the preparation procedure for the cryo-ET samples. Wild-type *E. coli* cells

689　(MG1655) were harvested in exponential phase, concentrated by centrifugation, deposited on the

21

690   grid and vitrified in liquid ethane. Using cryo-FIB milling, a thin lamella sample of thickness between

691   155 and 260 nm was obtained for the cryo-ET imaging.

692   B. Example section of the tomogram.

693   C. Comparison between the reference ribosome structure (gray) and the averaged structure (yellow)

694   derived from ribosomes localized in the lamella tomogram shown in panel B. An *E. coli* 70S ribosome

695   structure (EMD-20173) was used as the reference (Fu et al., 2019). See also Video S4 for a 3D

696   overview.

697   D. Maps showing localized ribosome structures (yellow) with the positions and orientations

698   determined in the tomogram shown in panel B.

699   E. Probability density maps of ribosome structures localized in the tomogram in panel B. The top

700   represents the probability density map of the localizations of ribosomes determined from the

701   tomogram. The map was constructed as a 2D histogram of the ribosome positions in the XY-plane.

702   The bottom map was obtained after Gaussian smoothing (σ = 1.2 pixel, 21 nm) of the top map to more

703   clearly show subcellular regions with high and low density in ribosomes.

704   See also Figure S4, Video S3 and Video S4.

705

706   **Figure 7. Pixel intensity correlation between DNA and ribosome fluorescence signals**

707   A. Fluorescence micrographs showing an example cell (CJW7020) with a strong negative correlation

708   (Spearman's ρ = -0.89) between the DNA and ribosome fluorescence signals. The cell outlines are

709   depicted as white solid lines, whereas the nucleoid outlines are shown as either black or white dash

710   lines. The images are shown using either the conventional gray scale or a color scale. The bottom row

711   shows only the pixels enclosed well within the nucleoid, at least two pixels away from the nucleoid

712   outline (STAR Methods). These pixels were used for the correlation calculation.

713   B. Similar to panel A, except for showing an example cell with a more common negative correlation

714   (Spearman's ρ = -0.60) between DNA and ribosome fluorescence signals.

715   C. Scatter plot showing the pixel intensity correlation between DAPI and L1-msfGFP signals obtained

716   in the cell shown in panel A.

717   D. Similar to C, except for showing the corresponding pixel intensity correlation in the cell shown in

718   panel B.

719   E. Probability density function of pixel intensity correlations calculated among the cell population (*n*

720   = 1,126).

721

722

723   **Figure 8. Chromosome compaction in different types of solvent.**

724   Bar graph showing the mean volume of 1,000 simulated chromosomes in each type of solvent. The

725   error bars represent the 95% confidence interval of the mean. The inset shows a comparison

726   between the volume of the nucleoid observed in the B-period *E. coli* cells (see Figure 2C) and the

727   volume calculated for simulated chromosomes (n = 1,000) in the poor solvent.

728   See also Video S5.

729

Supplemental figure legends

731   **Figure S1. Related to Figure 2. Comparison of DNA concentration measurements at 30°C and**

732   **37°C growth temperatures.**

733   Probability density functions of the average DNA concentrations estimated within the nucleoid

734   region in B-period cells (CJW6324) grown at either 30°C (green) or 37°C (red).

735

736   **Figure S2. Related to Figure 3. Example GFP-μNS particles of various sizes.**

737   Each panel shows a GFP fluorescence image of an *E.* coli cell (CJW4617). The GFP-μNS particles

738   appeared as distinct bright spots. The particle size is indicated in the upper right corner. The green

739   and yellow outlines are the cell and nucleoid contours detected by the Oufti software package.

740

741   **Figure S3. Related to Figure 5. Monte Carlo simulations of *E. coli* chromosomes.**

742   A. Six examples of distance maps indicating the spatial separation between any two loci along

743   simulated chromosomes in a poor solvent (v = 0.36). Each map is the result of averaging 10 randomly

744   selected simulated chromosomes.

745   B. Distance maps obtained by averaging 100 simulated chromosomes in a poor (v = 0.36), ideal (v =

746   0.50) and good solvent (v = 0.58). Same as Figure 5E, except for showing the distance maps for the

747   full simulated chromosomes.

748   C. Scaling between the number of segments and the normalized R_g of simulated chromosomes in

749   different types of solvent. For a better comparison in the scaling, the R_g of the simulated

750   chromosomes of different numbers of segments were normalized by the R_g of the chromosome with

751   10 segments. Each point is based on the average of 200 simulated chromosomes. Note that the scaling

752   was only shown for small length scales because the excluded volume interactions are screened for

753   polymers at large length scales. As a result, the scaling exponent becomes 0.5, regardless of the

754   solvent quality (Rubinstein, 2003).

755

756 **Figure S4. Related to Figure 6. Localization of ribosomes using cryo-ET**

757 A. Representative scanning electron microscope (SEM) image showing the *E. coli* cells on the grid

758 before the cryo-FIB milling.

759 B. Top view of the SEM image showing a lamella after the final polishing in cryo-FIB milling.

760 C. From left to right, each panel represents the same tomogram section overlaid with the ribosomes

761 identified by the initial 3D template search, after the removal of structures in the false class, and after

762 the removal of duplicate structures. In each case, the number of localized ribosome structures (*n*) is

763 indicated in the top right, and their positions are marked by the green circles.

764 D. Representative structures in the true and false classes during classification of the candidate 70S

765 ribosome structures found in the 3D template search.

766 E. Additional examples of probability density maps of ribosome structures localized in tomograms.

767 All maps were Gaussian smoothed (σ = 1.2 pixel, 21 nm) for easier visualization of the ribosome

768 regions of low and high densities.

769

770 # STAR Methods

771 ## Strains and growth conditions

772 This study used the following published strains. MG1655 (F-lambda- *ilvG- rfb*-50 *rph*-1) was used as

773 a wild-type *E. coli* strain (Jensen, 1993). Strain CJW6324 (MG1655 *seqA*::*seqA-mcherry ftsZ*::*ftsZ-*

774 *venus^{SW}*) was used to separate the cell population into three distinct groups that corresponded to the

775 cells in the B, C and D periods (Gray et al., 2019). Strain CJW6340 (BL21 Star (DE3) pET29b+ I3-01-

776 sfgfp) was obtained as a kind gift from David Baker's laboratory at the University of Washington (Hsia

777 et al., 2016). In this strain, the artificially designed protein I3-01 fused to superfolder GFP (I3-

778 01(ctGFP)) was produced from the pET29b+ plasmid in BL21 Star (DE3) *E. coli* cells. I3-01(ctGFP)

779 assembles into dodecahedron nanocage particles (Hsia et al., 2016). Strain CJW4617 (MG1655

780 Δ*lacZYA*::*gfp-μNS*) produces GFP-μNS particles of tunable sizes in response to IPTG induction (Parry

781 et al., 2014). Strain CJW7020 (MG1655 *rplA*::*rplA-msfgfp*) was used to investigate the pixel intensity

782 correlation between DNA and ribosome fluorescence signals (Gray et al., 2019).

783

784 To obtain steady-state growth conditions, a sample of an overnight liquid cell culture in stationary

785 phase was diluted by a factor of at least 10,000 in the corresponding fresh growth medium. The

786 culture was then allowed to grow in an incubator shaker (New Brunswick Innova 44), at the indicated

787 temperature, to reach an optical density at 600 nm (OD_{600}) of 0.1-0.3 prior to microscopy.

788

24

789

Light microscopy and image analysis

791 Unless otherwise specified, all exponentially growing cells were imaged on 1% agarose pads
792 supplemented with growth medium. When appropriate, cultures were incubated with 1 μg/ml 4′,6-
793 diamidino-2-phenylindole (DAPI) for 15 min in growth medium prior to imaging on agarose pads.
794 Phase contrast and epifluorescence imaging were performed on a Nikon Eclipse Ti-E microscope
795 equipped with a phase contrast Nikon CFI Plan Apo DM Lambda 100x oil objective (NA = 1.45), and
796 a SOLA light engine (Lumencor). A Ph3 phase contrast ring was used. The following Chroma filters
797 were used for epifluorescence imaging: DAPI (excitation D390/22x, dichroic T425lpxr, emission
798 ET460/50m), GFP (excitation ET470/40x, dichroic T495lpxr, emission ET525/50m),
799 mCherry/TexasRed (excitation ET560/40x, dichroic T585lp, emission ET630/75m). The microscope
800 was controlled by the NIS-Elements AR software.

801

802 Using the open source software Oufti (Paintdakhi et al., 2016), cell and nucleoid outlines were
803 constructed based on the phase contrast and epifluorescence images, respectively. When
804 appropriate, cells were classified into the B, C and D cell-cycle periods based on two cell features:
805 SeqA-mCherry pattern and cell area, as described before (Gray et al., 2019).

806

Derivation of the nucleoid mesh size

808 The correlation length ξ (i.e., mesh size) of a semidilute polymer solution is defined as $\xi =$
809 $R_g(c^*/c)^{\nu/(3\nu-1)}$ (Cooper et al., 1991; Dasgupta et al., 2002; Gennes, 1979; Rubinstein, 2003), where
810 R_g is the radius of gyration, c is the polymer concentration, and ν is the Flory exponent. The overlap
811 concentration c^*, above which polymer segments overlap to form a mesh can be written as $c^* =$
812 $3M_w Nb/(4\pi R_g^3 N_A l_{\text{base}})$ (Mutch et al., 2007; Ramakrishnan et al., 2002), where M_w is the average
813 molecular weight of the base pair (650 g/mol) (Lee et al., 2012; Peale et al., 1989; Ratilainen et al.,
814 2001), N is the number of polymer segments, b is the Kuhn length, l_{base} is the size of a base pair (0.34
815 nm) (Diekmann et al., 1982; Yonemura and Maeda, 1982), and N_A is the Avogadro's number. For a
816 circular polymer, $R_g = (\sqrt{3}/6)bN^\nu$ (Rubinstein, 2003). Plugging both the R_g and c^* into the above
817 definition, we have $\xi = (\sqrt{3}/6)bN^\nu [18\sqrt{3}M_w Nb/(\pi b^3 N^{3\nu} N_A l_{\text{base}} c)]^{\nu/(3\nu-1)}$, which can be simplified
818 to yield Eq. 1 above: $\xi = (\sqrt{3}/6)b^{(\nu-1)/(3\nu-1)}[18\sqrt{3}M_w/(\pi c N_A l_{\text{base}})]^{\nu/(3\nu-1)}$. To verify the dimension
819 of this result, we note the term $18\sqrt{3}M_w/(\pi c N_A l_{\text{base}})$ has a dimension of area. Since b has a
820 dimension of length and $(\nu-1)/(3\nu-1) + 2\nu/(3\nu-1) = 1$, ξ correctly has a dimension of length.

25

821

Estimation of the average DNA concentration within nucleoids of _E. coli_ in the B period

E. coli strain CJW6324 was grown at 37°C in M9 minimal medium supplemented with glycerol (0.2%). To estimate the average DNA concentration within the nucleoid regions, B-period cells (with a single chromosome) were first identified (see above). Given that the average molecular weight of a nucleotide base pair is 650 g/mol (Lee et al., 2012; Peale et al., 1989; Ratilainen et al., 2001) and the _E. coli_ genome size is about 4.6 million base pairs (Blattner et al., 1997), the total DNA mass in a single chromosome is around 5 femtograms. The nucleoid volume was estimated as $V_\text{nucleoid} = V_\text{cell}(A_\text{nucleoid}/A_\text{cell})^{3/2}$, where V_nucleoid, V_cell, A_nucleoid, A_cell are the volumes and areas of the nucleoid and cell. The cell volume was calculated by accumulating the volume of slices defined by neighboring pairs of points along the cell outlines (Paintdakhi et al., 2016) (see also documentation on oufti.org). The nucleoid and cell areas were calculated by summing up the areas of the polygons defined by the nucleoid and cell outlines. The power 3/2 was used to convert the estimated nucleoid area fraction into a volume fraction. The nucleoid volume estimation was performed at the single-cell level, as was the DNA concentration calculation, which was simply a division between the estimated DNA mass and the nucleoid volume.

837

Estimation of the average DNA concentration within nucleoids of _E. coli_ in nutrient-rich conditions

Bulk studies using the diphenylamine colorimetric assay and cell counting reported that the average DNA mass per cell under nutrient-rich conditions, glucose, glucose plus casamino acids and rich defined medium plus glucose as carbon sources, were around 10, 14 and 30 fg, respectively (Basan et al., 2015). The average cell sizes among these growth conditions (i.e. 2.32, 3.33, 6.60 μm^3, respectively) were also shown to scale linearly with the average DNA mass per cell (Basan et al., 2015). Taking into consideration of the strong scaling between the nucleoid size and cell size (Gray et al., 2019), we estimated the average DNA concentration within the nucleoid to be 7.3, 7.1 and 7.7 mg/ml under these three nutrient-rich growth conditions. Therefore, when taken together, the DNA concentration within the nucleoid among these nutrient-rich conditions is 7.4 ± 0.2 mg/ml.

849

Single-particle tracking experiments

GFP-tagged nanocage particles were produced through basal expression of the GFP-tagged protein subunit I3-01 in _E. coli_ cells (CJW6340) grown at 30°C in M9 minimal medium supplemented with glycerol (0.2%), casamino acids (0.1%) and thiamine (1 μg/ml). Phase contrast images were taken

26

854   first to define cell outlines. Time-lapse fluorescence images were then acquired at a frame rate of 100

855   ms. Nanocage particles were localized and tracked using the MATLAB class SPT (see supplementary

856   code). Briefly, an image was first smoothed by a band-pass filter. Potential regions containing the

857   particles were then segmented based on an intensity threshold. Based on the region sizes,

858   background noise pixels or particle clusters were filtered out. Within each of the remaining

859   segmented regions, the brightest pixel was located. On the brightest pixel and its eight surrounding

860   pixels, the pixel intensities were fitted by a 2D Gaussian distribution, whose center was taken as the

861   estimated particle position. The particle locations were linked into trajectories using an algorithm

862   described previously (Crocker and Grier, 1996). The 2D mean squared displacements (MSD) plot

863   were calculated as $\text{MSD}(\tau) = \langle (r(t+\tau) - r(t))^2 \rangle$, where τ is a given time delay and $r(t)$ and

864     $r(t+\tau)$ denote the particle positions before and after the given time delay. Similarly, GFP-µNS

865   particles were produced through IPTG induction (50-200 µM) for a duration of 30-120 min, in *E. coli*

866   cells (CJW4617) grown at 30°C in M9 minimal medium supplemented with glycerol (0.2%), casamino

867   acids (0.1%) and thiamine (1 µg/ml). GFP-µNS particles were detected using SpotFinder (Sliusarenko

868   et al., 2011). Particle positions of both nanocage-GFP and GFP-µNS particles relative to the cell

869   coordinates were calculated using the function projectToMesh in Oufti and normalized by cell width

870   and length. The relative particle positions were used to generate histograms to demonstrate the

871   probability density of relative particle locations inside the cell.

872

873   **Estimation of GFP-µNS particle sizes**

874   The size estimation of the GFP- µNS particles was performed as previously described (Parry et al.,

875   2014). This method establishes a relation between the fluorescence intensity (I) of GFP-µNS particles

876   and their absolute sizes (d). The particle fluorescence intensity (I) was calculated by integrating the

877   volume below the fitting bivariate normal distribution that was used to determine the particle

878   location: $I = 2\pi A \sigma_x \sigma_y$, where A is the amplitude of the fitting distribution, and σ_x, σ_y are the

879   standard deviations of the distribution in X and Y dimensions, respectively. Assuming the total

880   fluorescence intensity of a particle is proportional to its volume, and the volume is a cubic function

881   of its size (e.g., for a sphere), we further calculated the cubic root of the fluorescence intensity: $\sqrt[3]{I}$.

882

883   The absolute sizes of GFP-µNS particles were estimated as previously described (Parry et al., 2014).

884   Briefly, cells expressing GFP-µNS were lysed with T7 phages, resulting in the release of the GFP-µNS

885   particles in solution. Cell debris were removed by centrifugation at 4,000 g. Released GFP-µNS

886   particles were then mixed with fluorescent microspheres of known nominal size (110 nm,

27

887   FluoSpheres F8803, Invitrogen), and their diffusion coefficients were determined using single

888   particle tracking microscopy. We defined the fluorescence-derived relative particle size $d_{rel} =$

889    $\sqrt[3]{I/\langle I_{fluo}\rangle}$ for the GFP-μNS particles, where $\langle I_{fluo}\rangle$ denotes the average fluorescence intensity of the

890   fluorescent microspheres. Based on the Stokes-Einstein equation, the relative particle size and the

891   corresponding diffusion coefficient is inversely proportional: $D = kT/(3\pi\eta d_{rel})$, where k is the

892   Boltzmann constant, T is the absolute temperature, and η is the viscosity of the solution. The absolute

893   sizes of the GFP-μNS particles were estimated as $d = d_{fluo}D_{fluo}\alpha/D$, where d_{fluo} = 110 nm and $\alpha =$

894   d/d_{rel} is a calibration constant, which was found to be 685 nm.

895

896   **Monte Carlo simulation of chromosome conformation**

897   The entire *E. coli* chromosome (4.6 million base pairs, contour length = 1564 μm) was modeled as a

898   chain of 26,066 segments, each of which has a length of 60 nm (to reflect the assumed Kuhn length).

899   To achieve the experimentally determined average DNA concentration within the nucleoid region,

900   we confined the entire chromosome within a spherocylindrical space with a volume (0.70 μm³) equal

901   to the experimentally observed average nucleoid volume in B-period cells. In an ideal solvent where

902   the net interaction between the polymer and the solvent is neutral, there is no preference for a

903   segment on the polymer to interact more or less with other segments. In the simulation, at the end of

904   each step, a next-step segment was uniformly sampled from a spherical surface, the center and radius

905   of which are the end of the current step and the assumed Kuhn length, respectively. For a polymer in

906   a poor or good solvent, the segments on the polymer chain 'prefer' interacting among themselves

907   (poor solvent) or with the solvent (good solvent). To model the inter-segmental attraction and

908   repulsion, instead of sampling the next-step segments uniformly anywhere on the spherical surface,

909   restrictions were applied on the range of inclination and azimuth of the spherical surface from which

910   next-step segments (i.e., angles between the consecutive segments) could be sampled. By verifying

911   the power-law scaling between the number of segments and the radius of gyration of the simulated

912   chromosomes, the inter-segmental angles were constrained within empirically determined ranges

913   (Figure S3C). Specifically, we found that the Flory exponents (0.36 and 0.58) could be achieved when

914   the inter-segmental angles were constrained to be greater than $11\pi/18$ and smaller than $\pi/2$,

915   respectively.

916

917   Similarly, in order to compare the degree of chromosome compaction as a result of different types of

918   solvent, the *E. coli* chromosome was simulated in free space 1,000 times for each type of the solvent.

919   The radius of gyration of each simulated chromosome was calculated as $R_g^2 = \frac{1}{N}\sum_i^N (r_i - r_{mean})^2$,

28

920 where R_g is the radius of gyration, r_i is position of i-th segment, r_{mean} is the average position of all

921 segments and N is the total number of segments. To account for the circular geometry of the *E. coli*

922 chromosome, the resulted R_g was divided by a factor of $\sqrt{2}$ to get R'_g. The volume of the simulated

923 nucleoid in each type of solvent was calculated as $V = \frac{4}{3}\pi\left(R'_g\right)^3$.

924

Construction of distance maps for simulated DNA segments

926 The simulated chromosomes were binned by approximately 10 kb (56 DNA segments), and the

927 average positions of the segments within each bin were calculated. The binning was applied to reduce

928 the computational complexity of calculating the pair distance between DNA segments by more than

929 three orders of magnitude. A matrix of pair distances, where the i-th row and j-th column represent

930 the Euclidean distance between the i-th and j-th bins, was constructed for every simulated

931 chromosome. A chosen number (10 or 100) of such matrices were averaged together to generate

932 distance maps representing the average pair distances between the binned segments, which were

933 then visualized as images in which the individual pixels correspond to the distances.

934

Preparation of the cryo-EM grids

936 *E. coli* wild type cells (MG1655) were grown at 37°C in M9 minimal medium supplemented with

937 glucose (0.2%), casamino acids (1%) and thiamine (1 µg/ml). Nutrient-rich growth conditions were

938 chosen over nutrient-poor condition to increase the intracellular concentration of ribosomes (Dai et

939 al., 2016; Forchhammer and Lindahl, 1971; Phillips et al., 1969; Varricchio and Monier, 1971) thereby

940 decreasing the likelihood that any observed heterogeneity in ribosome distribution in the cell is due

941 to random clustering. Cells were then harvested and concentrated between 30- and 150-fold by

942 centrifugation (6,000 g for 5 min). The concentrated culture sample was deposited onto freshly glow-

943 discharged holey carbon grids (Quantifoil). The grids were then blotted with the filter paper for ~3-

944 5 s before getting plunge-frozen into liquid ethane, using a custom gravity-driven plunger apparatus

945 described previously (Liu et al., 2009; Zhao et al., 2013).

946

Cryo-FIB milling

948 The plunge-frozen grids were clipped into cryo-FIB AutoGrids and mounted into the specimen

949 shuttle under liquid nitrogen. An Aquilos cryo-FIB system (Thermo Fisher Scientific) was used to mill

950 the samples to produce thin lamellae. The samples were first sputter-coated with Pt (1 kV, 15 mA, 15

951 s) to improve the overall sample conductivity, and then were deposited by an organometallic Pt layer

952   (4-5 μm thick) using the gas injection system for the sample protection. Lamellae were produced

953   using the gallium ion beam at 30 kV with stage tilt angle around 17˚. The ion beam current was

954   reduced according to the lamella thickness (t) during the milling process: 0.5 nA for t ≥ 3 μm, 0.3 nA

955   for t ≥ 1 μm, 0.1 nA for t ≥ 700 nm, 0.05/0.03 nA for final polishing. Afterwards, a thin Pt layer was

956   sputter-coated (1 kV, 10 mA, 5 s) on the lamella to prevent possible charging issue during the cryo-

957   ET imaging.

958

959   Cryo-ET data acquisition and tomogram reconstruction

960   The cryo-FIB lamellae were transferred to a 300 kV Titan Krios electron microscope (Thermo Fisher

961   Scientific) equipped with a Direct Electron Detector and energy filter (Gatan). The program SerialEM

962   (Mastronarde, 2005) was used to collect single-axis tilt series around -6 μm defocus, with a

963   cumulative dose of ~100 e$^-$/Å covering angles from -60° to 60° (2° tilt step). Images were acquired

964   at 26,000× magnification with an effective pixel size of 5.457 Å at the specimen level. All recorded

965   images were first drift corrected by the software MotionCor2 (Zheng et al., 2017) and then stacked

966   by the software package IMOD (Kremer et al., 1996). All tilt series were then aligned by IMOD with

967   the patching tracking method. The program Gctf (Zhang, 2016) was used to determine the defocus of

968   each tilt image in the aligned stacks, and the function "ctfphaseflip" in IMOD was used to perform the

969   contrast transfer function (CTF) correction for the tilt images. Tomograms were then reconstructed

970   in IMOD using the CTF-corrected and aligned stacks.

971

972   Ribosome localization in the cryo-ET tomograms

973   The software package emClarity (Himes and Zhang, 2018) was used to perform the 3D template

974   search to identify ribosomes from the tomograms. A low-pass filtered (~ 4-nm resolution) *E. coli* 70S

975   ribosome structure (Fu et al., 2019) was used as a reference for the template search (Figure S4C).

976   Initially, up to 15,000-20,000 sub-volumes were initially selected from each tomogram.

977   Subsequently, the 3D classification and alignment were applied to all sub-volumes by the software

978   package i3 (Winkler, 2007; Winkler et al., 2009) with no binning. Sub-volumes of the particles in the

979   false class were removed (Figure S4D). After that, for every pair of localized structures, the

980   separation distance between their center mass was calculated. Two structures in a pair were

981   considered duplicates, if the distance between their centers of mass was smaller than 20 nm, and the

982   structure that had a lower cross-correlation score with the global average structure was removed.

983   This process repeated itself until no duplicate structure was found. The program UCSF ChimeraX

984   (Goddard et al., 2018) was used for the 3D surface rendering of subtomogram average structure of

985　ribosome. The accuracy of the localization of ribosomes was verified by both visual inspection and
986　comparison of the average structure obtained from the localized ribosomes to the reference
987　structure.

988

989　**Pixel intensity correlation between the DNA and ribosome fluorescence signals**

990　*E. coli* cells (CJW7020) were grown at 37°C in M9 minimal medium supplemented with glucose
991　(0.2%), casamino acids (1%) and thiamine (1 μg/ml). The nucleoid was visualized through DAPI
992　straining. Fluorescence signals from DAPI and L1-msfGFP were acquired. The nucleoid outlines were
993　constructed using objectDetection in the software package Oufti (Paintdakhi et al., 2016). In order to
994　exclusively quantify the pixel intensity correlation *within* the nucleoid region, the nucleoid outlines
995　were shrunk by 2 pixels from the original boundaries using the built-in MATLAB function polybuffer.
996　The shrunk nucleoid outlines enclosed, on average, about 30% of the inner most pixels defined by
997　the original outlines. Image masks were constructed using the shrunk nucleoid outlines, and pixels
998　from both the DAPI and GFP images were extracted. Correlation scores (Spearman's ρ) were then
999　calculated between the intensities of DAPI and GFP pixels using the built-in MATLAB function corr.

1000

1001　**Supplemental video legends**

1002　**Video S1. Related to Figure 3. Diffusion of a 25-nm nanocage-GFP particle**

1003　This video shows an example trajectory of nanocage-GFP particle diffusing in the cytoplasm of an *E.*
1004　*coli* cell (CJW6340). The left panel shows the original GFP fluorescence signal from the particle, and
1005　the right panel shows the additional annotation based on the single-particle tracking results: the
1006　particle center was denoted by the red point, and the yellow tail represents a short trajectory
1007　indicating the particle positions within the last 5 frames.

1008

1009　**Video S2. Related to Figure 5. Simulated chromosomes in different types of solvent.**

1010　This video shows a 3D overview of chromosomes simulated in confinement of a spherocylinder with
1011　a volume equal to that of an average nucleoid (~0.7 μm³). From left to right, the solvent was assumed
1012　to be poor ($v = 0.36$), ideal ($v = 0.50$) and good ($v = 0.58$). In all three cases, the Kuhn length of the
1013　DNA was assumed to be 60 nm.

1014

1015　**Video S3. Related to Figure 6. Tomogram of the *E. coli* lamella**

1016　This video shows the tomogram of an *E. coli* lamella obtained after the FIB milling. The lamella had
1017　an average thickness of 155 nm, and 5,028 ribosomes were detected in it. Based on their

1018 corresponding positions and orientations identified in the analysis, the ribosome structures (colored

1019 yellow) were placed back into the tomogram for visual inspection. The video shows individual

1020 tomogram sections along the Z-axis.

1021

1022 **Video S4. Related to Figure 6. Comparison between the reference and the average structure of**

1023 **localized 70S ribosomes**

1024 This video shows a 3D comparison between the low-pass filtered (~3 nm resolution) reference

1025 structure (grey) obtained from (Fu et al., 2019) and the average structure (yellow) based on all

1026 ribosomes localized in the tomogram shown in Figure 6B and Video S3.

1027

1028 **Video S5. Related to Figure 8. Simulated chromosomes in free space in different types of**

1029 **solvent**

1030 This video shows a 3D overview of chromosomes simulated in free (unbound) space in different

1031 types of solvent. From top to bottom, the solvent was assumed to be poor ($v = 0.36$), ideal ($v = 0.50$)

1032 and good ($v = 0.58$). In all three cases, the Kuhn length of the DNA was assumed to be 60 nm

1033

Analysis and simulation code availability

1035 All code used for analysis in this study can be found at https://github.com/JacobsWagnerLab.

1036

References

1038 Adiciptaningrum, A., Osella, M., Moolman, M.C., Cosentino Lagomarsino, M., and Tans, S.J. (2015).
1039 Stochasticity and homeostasis in the *E. coli* replication and division cycle. Sci. Rep. *5*, 18261.

1040 Alatossava, T., Jütte, H., Kuhn, A., and Kellenberger, E. (1985). Manipulation of intracellular
1041 magnesium content in polymyxin B nonapeptide-sensitized *Escherichia coli* by ionophore
1042 A23187. J. Bacteriol. *162*, 413-419.

1043 Auge, S., Schmit, P.O., Crutchfield, C.A., Islam, M.T., Harris, D.J., Durand, E., Clemancey, M., Quoineaud,
1044 A.A., Lancelin, J.M., Prigent, Y., *et al.* (2009). NMR measure of translational diffusion and fractal
1045 dimension. Application to molecular mass measurement. J. Phys. Chem. B *113*, 1914-1918.

1046 Axpe, E., Chan, D., Offeddu, G.S., Chang, Y., Merida, D., Hernandez, H.L., and Appel, E.A. (2019). A
1047 multiscale model for solute diffusion in hydrogels. Macromolecules *52*, 6889-6897.

1048 Azam, T.A., Hiraga, S., and Ishihama, A. (2000). Two types of localization of the DNA-binding proteins
1049 within the *Escherichia coli* nucleoid. Genes Cells *5*, 613-626.

1050 Bakshi, S., Choi, H., Mondal, J., and Weisshaar, J.C. (2014). Time-dependent effects of transcription-
1051 and translation-halting drugs on the spatial distributions of the *Escherichia coli* chromosome and
1052 ribosomes. Mol. Microbiol. *94*, 871-887.

Bakshi, S., Siryaporn, A., Goulian, M., and Weisshaar, J.C. (2012). Superresolution imaging of ribosomes and RNA polymerase in live *Escherichia coli* cells. Mol. Microbiol. *85*, 21-38.

Basan, M., Zhu, M., Dai, X., Warren, M., Sévin, D., Wang, Y.P., and Hwa, T. (2015). Inflating bacterial cells by increased protein synthesis. Mol. Syst. Biol. *11*, 836.

Baumann, C.G., Smith, S.B., Bloomfield, V.A., and Bustamante, C. (1997). Ionic effects on the elasticity of single DNA molecules. Proc. Natl. Acad. Sci. USA *94*, 6185-6190.

Bernstein, J.A., Khodursky, A.B., Lin, P.H., Lin-Chao, S., and Cohen, S.N. (2002). Global analysis of mRNA decay and abundance in *Escherichia coli* at single-gene resolution using two-color fluorescent DNA microarrays. Proc. Natl. Acad. Sci. USA *99*, 9697-9702.

Blattner, F.R., Plunkett, G., 3rd, Bloch, C.A., Perna, N.T., Burland, V., Riley, M., Collado-Vides, J., Glasner, J.D., Rode, C.K., Mayhew, G.F.*, et al.* (1997). The complete genome sequence of *Escherichia coli* K-12. Science *277*, 1453-1462.

Bloomfield, V.A. (1997). DNA condensation by multivalent cations. Biopolymers *44*, 269-282.

Borochov, N., Eisenberg, H., and Kam, Z. (1981). Dependence of DNA conformation on the concentration of salt. Biopolymers *20*, 231-235.

Boublik, M. (1985). Structure of the *Escherichia coli* ribosome. Molecular cytology of *Escherichia coli*, N. Nanninga, ed. (Academic Press).

Brangwynne, C.P., Koenderink, G.H., MacKintosh, F.C., and Weitz, D.A. (2009). Intracellular transport by active diffusion. Trends Cell Biol. *19*, 423-427.

Bremer, H., and Dennis, P.P. (2008). Modulation of chemical composition and other parameters of the cell at different exponential growth rates. EcoSal Plus *3*.

Brendler, T., Abeles, A., and Austin, S. (1995). A protein that binds to the P1 origin core and the oriC 13mer region in a methylation-specific fashion is the product of the host seqA gene. EMBO Journal *14*, 4083-4089.

Broering, T.J., Arnold, M.M., Miller, C.L., Hurt, J.A., Joyce, P.L., and Nibert, M.L. (2005). Carboxyl-proximal regions of reovirus nonstructural protein μNS necessary and sufficient for forming factory-like inclusions. J. Virol. *79*, 6194.

Broering, T.J., Parker, J.S.L., Joyce, P.L., Kim, J., and Nibert, M.L. (2002). Mammalian reovirus nonstructural protein μNS forms large inclusions and colocalizes with reovirus microtubule-associated protein μ2 in transfected cells. J. Virol. *76*, 8285.

Cabrera, J.E., Cagliero, C., Quan, S., Squires, C.L., and Jin, D.J. (2009). Active transcription of rRNA operons condenses the nucleoid in *Escherichia coli*: examining the effect of transcription on nucleoid structure in the absence of transertion. J. Bacteriol. *191*, 4180-4185.

Cabrera, J.E., and Jin, D.J. (2003). The distribution of RNA polymerase in *Escherichia coli* is dynamic and sensitive to environmental cues. Mol. Microbiol. *50*, 1493-1505.

Cai, L.H., Panyukov, S., and Rubinstein, M. (2011). Mobility of nonsticky nanoparticles in polymer liquids. Macromolecules *44*, 7853-7863.

Carn, F., Boué, F., Djabourov, M., Steunou, N., Coradin, T., Livage, J., Floquet, S., Cadot, E., and Buhler, E. (2012). Biopolymer folding driven nanoparticle reorganization in bio-nanocomposites. Soft Matter *8*, 2930-2944.

Casassa, E.F. (1965). Some statistical properties of flexible ring polymers. J. Polym. Sci. A Gen. Pap. *3*, 605-614.

1095 Cayley, S., Lewis, B.A., Guttman, H.J., and Record, M.T. (1991). Characterization of the cytoplasm of
1096   *Escherichia coli* K-12 as a function of external osmolarity: implications for protein-DNA
1097   interactions in vivo. J. Mol. Biol. *222*, 281-300.

1098 Chen, H., Shiroguchi, K., Ge, H., and Xie, X.S. (2015). Genome-wide study of mRNA degradation and
1099   transcript elongation in *Escherichia coli*. Mol. Syst. Biol. *11*, 781.

1100 Chowdhury, C., Sinha, S., Chun, S., Yeates, T.O., and Bobik, T.A. (2014). Diverse bacterial
1101   microcompartment organelles. Microbiol. Mol. Biol. Rev. *78*, 438-468.

1102 Cooper, E.C., Johnson, P., and Donald, A.M. (1991). Probe diffusion in polymer solutions in the
1103   dilute/semi-dilute crossover regime: 1. Poly(ethylene oxide). Polymer *32*, 2815-2822.

1104 Cooper, S., and Helmstetter, C.E. (1968). Chromosome replication and the division cycle of *Escherichia
1105   coli* B/r. J. Mol. Biol. *31*, 519-540.

1106 Crocker, J.C., and Grier, D.G. (1996). Methods of digital video microscopy for colloidal studies. J.
1107   Colloid Interface Sci. *179*, 298-310.

1108 Cunha, S., Woldringh, C.L., and Odijk, T. (2001). Polymer-mediated compaction and internal dynamics
1109   of isolated *Escherichia coli* nucleoids. J. Struct. Biol. *136*, 53-66.

1110 Dai, X., Zhu, M., Warren, M., Balakrishnan, R., Patsalo, V., Okano, H., Williamson, J.R., Fredrick, K., Wang,
1111   Y.P., and Hwa, T. (2016). Reduction of translating ribosomes enables *Escherichia coli* to maintain
1112   elongation rates during slow growth. Nat. Microbiol. *2*, 16231.

1113 Dame, R.T. (2005). The role of nucleoid-associated proteins in the organization and compaction of
1114   bacterial chromatin. Mol. Microbiol. *56*, 858-870.

1115 Dame, R.T., Rashid, F.M., and Grainger, D.C. (2020). Chromosome organization in bacteria:
1116   mechanistic insights into genome structure and function. Nat. Rev. Genet. *21*, 227-242.

1117 Dasgupta, B.R., Tee, S.-Y., Crocker, J.C., Frisken, B.J., and Weitz, D.A. (2002). Microrheology of
1118   polyethylene oxide using diffusing wave spectroscopy and single scattering. Phys. Rev. E *65*,
1119   051505.

1120 de Vries, R. (2010). DNA condensation in bacteria: interplay between macromolecular crowding and
1121   nucleoid proteins. Biochimie *92*, 1715-1721.

1122 Deana, A., and Belasco, J.G. (2005). Lost in translation: the influence of ribosomes on bacterial mRNA
1123   decay. Genes Dev. *19*, 2526-2533.

1124 Diekmann, S., Hillen, W., Morgeneyer, B., Wells, R.D., and Pörschke, D. (1982). Orientation relaxation
1125   of DNA restriction fragments and the internal mobility of the double helix. Biophys. Chem. *15*,
1126   263-270-270.

1127 Dillon, S.C., and Dorman, C.J. (2010). Bacterial nucleoid-associated proteins, nucleoid structure and
1128   gene expression. Nat. Rev. Microbiol. *8*, 185-195.

1129 Dorman, C.J. (2019). DNA supercoiling and transcription in bacteria: a two-way street. BMC Mol. Cell
1130   Biol. *20*, 26.

1131 Dreyfus, M. (2009). Chapter 11 killer and protective ribosomes. Progress in Molecular Biology and
1132   Translational Science (Academic Press), pp. 423-466.

1133 Dworsky, P., and Schaechter, M. (1973). Effect of rifampin on the structure and membrane
1134   attachment of the nucleoid of *Escherichia coli*. J. Bacteriol. *116*, 1364-1374.

1135 Flyamer, I.M., Gassler, J., Imakaev, M., Brandao, H.B., Ulianov, S.V., Abdennur, N., Razin, S.V., Mirny,
1136   L.A., and Tachibana-Konwalski, K. (2017). Single-nucleus Hi-C reveals unique chromatin
1137   reorganization at oocyte-to-zygote transition. Nature *544*, 110-114.

1138 Forchhammer, J., and Lindahl, L. (1971). Growth rate of polypeptide chains as a function of the cell
1139   growth rate in a mutant of *Escherichia coli* 15. J. Mol. Biol. *55*, 563-568.

1140 Fu, Z., Indrisiunaite, G., Kaledhonkar, S., Shah, B., Sun, M., Chen, B., Grassucci, R.A., Ehrenberg, M., and
1141   Frank, J. (2019). The structural basis for release-factor activation during translation termination
1142   revealed by time-resolved cryogenic electron microscopy. Nat. Commun. *10*, 2579.

1143 Gennes, P.-G.d. (1979). Scaling concepts in polymer physics (Cornell University Press).

1144 Goddard, T.D., Huang, C.C., Meng, E.C., Pettersen, E.F., Couch, G.S., Morris, J.H., and Ferrin, T.E. (2018).
1145   UCSF ChimeraX: meeting modern challenges in visualization and analysis. Protein Sci. *27*, 14-25.

1146 Gray, W.T., Govers, S.K., Xiang, Y., Parry, B.R., Campos, M., Kim, S., and Jacobs-Wagner, C. (2019).
1147   Nucleoid size scaling and intracellular organization of translation across bacteria. Cell *177*, 1632-
1148   1648.e1620.

1149 Guettari, M., Gomati, R., and Gharbi, A. (2012). Determination of the Flory exponent by study of steady
1150   shear viscosity. J. Macromol. Sci. B *51*, 153-163.

1151 Guo, M., Ehrlicher, A.J., Jensen, M.H., Renz, M., Moore, J.R., Goldman, R.D., Lippincott-Schwartz, J.,
1152   Mackintosh, F.C., and Weitz, D.A. (2014). Probing the stochastic, motor-driven properties of the
1153   cytoplasm using force spectrum microscopy. Cell *158*, 822-832.

1154 Hammel, M., Amlanjyoti, D., Reyes, F.E., Chen, J.H., Parpana, R., Tang, H.Y., Larabell, C.A., Tainer, J.A.,
1155   and Adhya, S. (2016). HU multimerization shift controls nucleoid compaction. Sci. Adv. *2*,
1156   e1600650.

1157 Haran, G. (2012). How, when and why proteins collapse: the relation to folding. Curr. Opin. Struct.
1158   Biol. *22*, 14-20.

1159 Helgesen, E., Fossum-Raunehaug, S., Sætre, F., Schink, K.O., and Skarstad, K. (2015). Dynamic
1160   *Escherichia coli* SeqA complexes organize the newly replicated DNA at a considerable distance
1161   from the replisome. Nucleic Acids Res. *43*, 2730-2743.

1162 Henry, J.T., and Crosson, S. (2013). Chromosome replication and segregation govern the biogenesis
1163   and inheritance of inorganic polyphosphate granules. Mol. Biol. Cell *24*, 3177-3186.

1164 Himes, B.A., and Zhang, P. (2018). emClarity: software for high-resolution cryo-electron tomography
1165   and subtomogram averaging. Nat. Methods *15*, 955-961.

1166 Hobot, J.A., Villiger, W., Escaig, J., Maeder, M., Ryter, A., and Kellenberger, E. (1985). Shape and fine
1167   structure of nucleoids observed on sections of ultrarapidly frozen and cryosubstituted bacteria.
1168   J. Bacteriol. *162*, 960-971.

1169 Holmes, V.F., and Cozzarelli, N.R. (2000). Closing the ring: links between SMC proteins and
1170   chromosome partitioning, condensation, and supercoiling. Proc. Natl. Acad. Sci. USA *97*, 1322-
1171   1324.

1172 Hsia, Y., Bale, J.B., Gonen, S., Shi, D., Sheffler, W., Fong, K.K., Nattermann, U., Xu, C., Huang, P.S.,
1173   Ravichandran, R., *et al.* (2016). Design of a hyperstable 60-subunit protein dodecahedron.
1174   [corrected]. Nature *535*, 136-139.

Jensen, K.F. (1993). The *Escherichia coli* K-12 "wild types" W3110 and MG1655 have an rph frameshift mutation that leads to pyrimidine starvation due to low pyrE expression levels. J. Bacteriol. *175*, 3401-3407.

Jeon, C., Jung, Y., and Ha, B.-Y. (2017). A ring-polymer model shows how macromolecular crowding controls chromosome-arm organization in *Escherichia coli*. Sci. Rep. *7*, 11896-11896.

Joyeux, M. (2014). Equilibration of complexes of DNA and H-NS proteins on charged surfaces: A coarse-grained model point of view. J. Chem. Phys. *141*, 115102.

Jun, S. (2015). Chromosome, cell cycle, and entropy. Biophys. J. *108*, 785-786.

Kam, Z., Borochov, N., and Eisenberg, H. (1981). Dependence of laser light scattering of DNA on NaCl concentration. Biopolymers *20*, 2671-2690.

Kavenoff, R., and Bowen, B.C. (1976). Electron microscopy of membrane-free folded chromosomes from *Escherichia coli*. Chromosoma *59*, 89-101.

Kavenoff, R., and Ryder, O.A. (1976). Electron microscopy of membrane-associated folded chromosomes of *Escherichia coli*. Chromosoma *55*, 13-25.

Kellenberger, E., Ryter, A., and Sechaud, J. (1958). Electron microscope study of DNA-containing plasms. II. vegetative and mature phage DNA as compared with normal bacterial nucleoids in different physiological states. J. Biophys. Biochem. Cytol. *4*, 671-678.

Kramers, H.A. (1946). The behavior of macromolecules in inhomogeneous flow. J. Chem. Phys. *14*, 415-424.

Kremer, J.R., Mastronarde, D.N., and McIntosh, J.R. (1996). Computer visualization of three-dimensional image data using IMOD. J. Struct. Biol. *116*, 71-76.

Kuhn, A., and Kellenberger, E. (1985). Productive phage infection in *Escherichia coli* with reduced internal levels of the major cations. J. Bacteriol. *163*, 906-912.

Le Gall, A., Cattoni, D.I., Guilhas, B., Mathieu-Demazière, C., Oudjedi, L., Fiche, J.-B., Rech, J., Abrahamsson, S., Murray, H., Bouet, J.-Y.*, et al.* (2016). Bacterial partition complexes segregate within the volume of the nucleoid. Nat. Commun. *7*, 12107-12107.

Le, T.B., Imakaev, M.V., Mirny, L.A., and Laub, M.T. (2013). High-resolution mapping of the spatial organization of a bacterial chromosome. Science *342*, 731-734.

Le, T.B., and Laub, M.T. (2016). Transcription rate and transcript length drive formation of chromosomal interaction domain boundaries. EMBO J. *35*, 1582-1595.

Lee, C.K., Araki, N., Sowersby, D.S., and Lewis, L.K. (2012). Factors affecting chemical-based purification of DNA from Saccharomyces cerevisiae. Yeast *29*, 73-80.

Lewis, P.J., Thaker, S.D., and Errington, J. (2000). Compartmentalization of transcription and translation in Bacillus subtilis. EMBO J. *19*, 710-718.

Libby, E.A., Roggiani, M., and Goulian, M. (2012). Membrane protein expression triggers chromosomal locus repositioning in bacteria. Proc. Natl. Acad. Sci. USA *109*, 7445-7450.

Lioy, V.S., Cournac, A., Marbouty, M., Duigou, S., Mozziconacci, J., Espeli, O., Boccard, F., and Koszul, R. (2018). Multiscale structuring of the *E. coli* chromosome by nucleoid-associated and condensin proteins. Cell *172*, 771-783.e718.

36

1214   Liu, J., Lin, T., Botkin, D.J., McCrum, E., Winkler, H., and Norris, S.J. (2009). Intact flagellar motor of
1215   Borrelia burgdorferi revealed by cryo-electron tomography: evidence for stator ring curvature
1216   and rotor/C-ring assembly flexion. J. Bacteriol. *191*, 5026-5036.

1217   Lopez, P.J., Marchand, I., Yarchuk, O., and Dreyfus, M. (1998). Translation inhibitors stabilize
1218   *Escherichia coli* mRNAs independently of ribosome protection. Proc. Natl. Acad. Sci. USA *95*, 6067-
1219   6072.

1220   Lu, M., Campbell, J.L., Boye, E., and Kleckner, N. (1994). SeqA: A negative modulator of replication
1221   initiation in *E. coli*. Cell *77*, 413-426.

1222   Lusk, J.E., Williams, R.J.P., and Kennedy, E.P. (1968). Magnesium and the growth of *Escherichia coli*. J.
1223   Biol. Chem. *243*, 2618-2624.

1224   Ma, J., and Wang, M.D. (2016). DNA supercoiling during transcription. Biophys. Rev. *8*, 75-87.

1225   Macvanin, M., Edgar, R., Cui, F., Trostel, A., Zhurkin, V., and Adhya, S. (2012). Noncoding RNAs binding
1226   to the nucleoid protein HU in *Escherichia coli*. J. Bacteriol. *194*, 6046-6055.

1227   Mantelli, S., Muller, P., Harlepp, S., and Maaloum, M. (2011). Conformational analysis and estimation
1228   of the persistence length of DNA using atomic force microscopy in solution. Soft Matter *7*, 3412-
1229   3416.

1230   Marbouty, M., Cournac, A., Flot, J.F., Marie-Nelly, H., Mozziconacci, J., and Koszul, R. (2014).
1231   Metagenomic chromosome conformation capture (meta3C) unveils the diversity of chromosome
1232   organization in microorganisms. eLife *3*, e03318.

1233   Marbouty, M., Le Gall, A., Cattoni, D.I., Cournac, A., Koh, A., Fiche, J.B., Mozziconacci, J., Murray, H.,
1234   Koszul, R., and Nollmann, M. (2015). Condensin- and replication-mediated bacterial chromosome
1235   folding and origin condensation revealed by Hi-C and super-resolution imaging. Mol. Cell *59*, 588-
1236   602.

1237   Mason, D.J., and Powelson, D.M. (1956). Nuclear division as observed in live bacteria by a new
1238   technique. J. Bacteriol. *71*, 474-479.

1239   Mastronarde, D.N. (2005). Automated electron microscope tomography using robust prediction of
1240   specimen movements. J. Struct. Biol. *152*, 36-51.

1241   Molina, F., and Skarstad, K. (2004). Replication fork and SeqA focus distributions in *Escherichia coli*
1242   suggest a replication hyperstructure dependent on nucleotide metabolism. Mol. Microbiol. *52*,
1243   1597-1612.

1244   Moncany, M.L.J., and Kellenberger, E. (1981). High magnesium content of *Escherichia coli* B.
1245   Experientia *37*, 846-847.

1246   Mutch, K.J., van Duijneveldt, J.S., and Eastoe, J. (2007). Colloid–polymer mixtures in the protein limit.
1247   Soft Matter *3*, 155-167.

1248   Nagano, T., Lubling, Y., Stevens, T.J., Schoenfelder, S., Yaffe, E., Dean, W., Laue, E.D., Tanay, A., and
1249   Fraser, P. (2013). Single-cell Hi-C reveals cell-to-cell variability in chromosome structure. Nature
1250   *502*, 59-64.

1251   Nagano, T., Lubling, Y., Varnai, C., Dudley, C., Leung, W., Baran, Y., Mendelson Cohen, N., Wingett, S.,
1252   Fraser, P., and Tanay, A. (2017). Cell-cycle dynamics of chromosomal organization at single-cell
1253   resolution. Nature *547*, 61-67.

1254   Nicolai, T., and Mandel, M. (1989). The ionic strength dependence of the second virial coefficient of
1255   low molar mass DNA fragments in aqueous solutions. Macromolecules *22*, 438-444.

1256 Odijk, T. (1998). Osmotic compaction of supercoiled DNA into a bacterial nucleoid. Biophys. Chem.
1257   *73*, 23-29.

1258 Paintdakhi, A., Parry, B., Campos, M., Irnov, I., Elf, J., Surovtsev, I., and Jacobs-Wagner, C. (2016). Oufti:
1259   an integrated software package for high-accuracy, high-throughput quantitative microscopy
1260   analysis. Mol. Microbiol. *99*, 767-777.

1261 Parry, B.R., Surovtsev, I.V., Cabeen, M.T., O'Hern, C.S., Dufresne, E.R., and Jacobs-Wagner, C. (2014).
1262   The bacterial cytoplasm has glass-like properties and is fluidized by metabolic activity. Cell *156*,
1263   183-194.

1264 Pato, M.L., Bennett, P.M., and Von Meyenburg, K. (1973). Messenger ribonucleic acid synthesis and
1265   degradation in *Escherichia coli* during inhibition of translation. J. Bacteriol. *116*, 710-718.

1266 Peale, F.V., Jr., Ishibe, Y., Klinge, C.M., Zain, S., Hilf, R., and Bambara, R.A. (1989). Rapid purification of
1267   the estrogen receptor by sequence-specific DNA affinity chromatography. Biochemistry *28*, 8671-
1268   8675.

1269 Pelletier, J., Halvorsen, K., Ha, B.Y., Paparcone, R., Sandler, S.J., Woldringh, C.L., Wong, W.P., and Jun, S.
1270   (2012). Physical manipulation of the *Escherichia coli* chromosome reveals its soft nature. Proc.
1271   Natl. Acad. Sci. USA *109*, E2649-2656.

1272 Pettijohn, D.E., and Hecht, R. (1974). RNA molecules bound to the folded bacterial genome stabilize
1273   DNA folds and segregate domains of supercoiling. Cold Spring Harb. Symp. Quant. Biol. *38*, 31-41.

1274 Phillips, L.A., Hotham-Iglewski, B., and Franklin, R.M. (1969). Polyribosomes of *Escherichia coli*. II.
1275   Experiments to determine the in vivo distribution of polysomes, ribosomes and ribosomal
1276   subunits. J. Mol. Biol. *45*, 23-38.

1277 Piekarski, G. (1937). Zytologische Untersuchungen an Paratyphusund Coli Bakterien. Arch Mikrobiol
1278   *8*, 428-429.

1279 Porschke, D. (1986). Structure and dynamics of double helices in solution: modes of DNA bending. J.
1280   Biomol. Struct. Dyn. *4*, 373-389.

1281 Porschke, D. (1991). Persistence length and bending dynamics of DNA from electrooptical
1282   measurements at high salt concentrations. Biophys. Chem. *40*, 169-179.

1283 Qian, Z., Zhurkin, V.B., and Adhya, S. (2017). DNA-RNA interactions are critical for chromosome
1284   condensation in *Escherichia coli*. Proc. Natl. Acad. Sci. USA *114*, 12225-12230.

1285 Qiu, X., Andresen, K., Kwok, L.W., Lamb, J.S., Park, H.Y., and Pollack, L. (2007). Inter-DNA attraction
1286   mediated by divalent counterions. Phys. Rev. Lett. *99*, 038104.

1287 Racki, L.R., Tocheva, E.I., Dieterle, M.G., Sullivan, M.C., Jensen, G.J., and Newman, D.K. (2017).
1288   Polyphosphate granule biogenesis is temporally and functionally tied to cell cycle exit during
1289   starvation in Pseudomonas aeruginosa. Proc. Natl. Acad. Sci. USA *114*, E2440-e2449.

1290 Ramakrishnan, S., Fuchs, M., Schweizer, K.S., and Zukoski, C.F. (2002). Entropy driven phase
1291   transitions in colloid–polymer suspensions: tests of depletion theories. J. Chem. Phys. *116*, 2201-
1292   2212.

1293 Ramani, V., Deng, X., Qiu, R., Gunderson, K.L., Steemers, F.J., Disteche, C.M., Noble, W.S., Duan, Z., and
1294   Shendure, J. (2017). Massively multiplex single-cell Hi-C. Nat. Methods. *14*, 263-266.

1295 Ratilainen, T., Lincoln, P., and Norden, B. (2001). A simple model for gene targeting. Biophys. J. *81*,
1296   2876-2885.

1297 Reyes-Lamothe, R., Tran, T., Meas, D., Lee, L., Li, A.M., Sherratt, D.J., and Tolmasky, M.E. (2014). High-
1298   copy bacterial plasmids diffuse in the nucleoid-free space, replicate stochastically and are
1299   randomly partitioned at cell division. Nucleic Acids Res. *42*, 1042-1051.

1300 Robinow, C., and Kellenberger, E. (1994). The bacterial nucleoid revisited. Microbiol. Rev. *58*, 211-
1301   232.

1302 Roe, A.J., McLaggan, D., Davidson, I., O'Byrne, C., and Booth, I.R. (1998). Perturbation of anion balance
1303   during inhibition of growth of *Escherichia coli* by weak acids. J. Bacteriol. *180*, 767-772.

1304 Rubinstein, M. (2003). Polymer physics, R.H. Colby, ed. (Oxford University Press).

1305 Sanamrad, A., Persson, F., Lundius, E.G., Fange, D., Gynna, A.H., and Elf, J. (2014). Single-particle
1306   tracking reveals that free ribosomal subunits are not excluded from the *Escherichia coli* nucleoid.
1307   Proc. Natl. Acad. Sci. USA *111*, 11413-11418.

1308 Schneider, E., Blundell, M., and Kennell, D. (1978). Translation and mRNA decay. Mol. Gen. Genet. *160*,
1309   121-129.

1310 Schultz, S.G., Wilson, N.L., and Epstein, W. (1962). Cation transport in *Escherichia coli*. II. Intracellular
1311   chloride concentration. J. Gen. Physiol. *46*, 159-166.

1312 Selinger, D.W., Saxena, R.M., Cheung, K.J., Church, G.M., and Rosenow, C. (2003). Global RNA half-life
1313   analysis in *Escherichia coli* reveals positional patterns of transcript degradation. Genome Res. *13*,
1314   216-223.

1315 Sharpe, M.E., Hauser, P.M., Sharpe, R.G., and Errington, J. (1998). Bacillus subtilis cell cycle as studied
1316   by fluorescence microscopy: constancy of cell length at initiation of DNA replication and evidence
1317   for active nucleoid partitioning. J. Bacteriol. *180*, 547-555.

1318 Shendruk, T.N., Bertrand, M., de Haan, H.W., Harden, J.L., and Slater, G.W. (2015). Simulating the
1319   entropic collapse of coarse-grained chromosomes. Biophys. J. *108*, 810-820.

1320 Slater, S., Wold, S., Lu, M., Boye, E., Skarstad, K., and Kleckner, N. (1995). *E. coli* SeqA protein binds
1321   oriC in two different methyl-modulated reactions appropriate to its roles in DNA replication
1322   initiation and origin sequestration. Cell *82*, 927-936.

1323 Sliusarenko, O., Heinritz, J., Emonet, T., and Jacobs-Wagner, C. (2011). High-throughput, subpixel
1324   precision analysis of bacterial morphogenesis and intracellular spatio-temporal dynamics. Mol.
1325   Microbiol. *80*, 612-627.

1326 Sobel, E.S., and Harpst, J.A. (1991). Effects of Na+ on the persistence length and excluded volume of
1327   T7 bacteriophage DNA. Biopolymers *31*, 1559-1564.

1328 Spahn, C., Endesfelder, U., and Heilemann, M. (2014). Super-resolution imaging of *Escherichia coli*
1329   nucleoids reveals highly structured and asymmetric segregation during fast growth. J. Struct. Biol.
1330   *185*, 243-249.

1331 Spahn, C.K., Glaesmann, M., Grimm, J.B., Ayala, A.X., Lavis, L.D., and Heilemann, M. (2018). A toolbox
1332   for multiplexed super-resolution imaging of the *E. coli* nucleoid and membrane using novel
1333   PAINT labels. Sci. Rep. *8*, 14768.

1334 Spurio, R., Durrenberger, M., Falconi, M., La Teana, A., Pon, C.L., and Gualerzi, C.O. (1992). Lethal
1335   overproduction of the *Escherichia coli* nucleoid protein H-NS: ultramicroscopic and molecular
1336   autopsy. Mol. Gen. Genet. *231*, 201-211.

1337 Stevens, T.J., Lando, D., Basu, S., Atkinson, L.P., Cao, Y., Lee, S.F., Leeb, M., Wohlfahrt, K.J., Boucher, W.,
1338   O'Shaughnessy-Kirwan, A., *et al.* (2017). 3D structures of individual mammalian genomes studied
1339   by single-cell Hi-C. Nature *544*, 59-64.

1340 Stracy, M., Lesterlin, C., Garza de Leon, F., Uphoff, S., Zawadzki, P., and Kapanidis, A.N. (2015). Live-
1341   cell superresolution microscopy reveals the organization of RNA polymerase in the bacterial
1342   nucleoid. Proc. Natl. Acad. Sci. USA *112*, E4390-4399.

1343 Sun, Q., and Margolin, W. (2004). Effects of perturbing nucleoid structure on nucleoid occlusion-
1344   mediated toporegulation of FtsZ ring assembly. J. Bacteriol. *186*, 3951-3959.

1345 Surovtsev, I.V., and Jacobs-Wagner, C. (2018). Subcellular organization: a critical feature of bacterial
1346   cell replication. Cell *172*, 1271-1293.

1347 Tan, L., Xing, D., Chang, C.H., Li, H., and Xie, X.S. (2018). Three-dimensional genome structures of single
1348   diploid human cells. Science *361*, 924-928.

1349 Tan, L., Xing, D., Daley, N., and Xie, X.S. (2019). Three-dimensional genome structures of single
1350   sensory neurons in mouse visual and olfactory systems. Nat. Struct. Mol. Biol. *26*, 297-307.

1351 Trun, N.J., and Marko, J.F. (1998). Architecture of a bacterial chromosome. Asm News *64*, 276-283.

1352 Tseng, Y., Lee, J.S., Kole, T.P., Jiang, I., and Wirtz, D. (2004). Micro-organization and visco-elasticity of
1353   the interphase nucleus revealed by particle nanotracking. J. Cell Sci. *117*, 2159-2167.

1354 Val, M.E., Marbouty, M., de Lemos Martins, F., Kennedy, S.P., Kemble, H., Bland, M.J., Possoz, C., Koszul,
1355   R., Skovgaard, O., and Mazel, D. (2016). A checkpoint control orchestrates the replication of the
1356   two chromosomes of Vibrio cholerae. Sci. Adv. *2*, e1501914.

1357 van Helvoort, J.M., Kool, J., and Woldringh, C.L. (1996). Chloramphenicol causes fusion of separated
1358   nucleoids in *Escherichia coli* K-12 cells and filaments. J. Bacteriol. *178*, 4289-4293.

1359 Varricchio, F., and Monier, R. (1971). Ribosome patterns in *Escherichia coli* growing at various rates.
1360   J. Bacteriol. *108*, 105-110.

1361 Verma, S.C., Qian, Z., and Adhya, S.L. (2019). Architecture of the *Escherichia coli* nucleoid. PLoS Genet.
1362   *15*, e1008456-e1008456.

1363 Verschoor, A., Frank, J., and Boublik, M. (1985). Investigation of the 50 S ribosomal subunit by
1364   electron microscopy and image analysis. J. Ultrastruct. Res. *92*, 180-189.

1365 Waigh, T.A., Ober, R., Williams, C.E., and Galin, J.-C. (2001). Semidilute and concentrated solutions of
1366   a solvophobic polyelectrolyte in nonaqueous solvents. Macromolecules *34*, 1973-1980.

1367 Waldminghaus, T., Weigel, C., and Skarstad, K. (2012). Replication fork movement and methylation
1368   govern SeqA binding to the *Escherichia coli* chromosome. Nucleic Acids Res. *40*, 5465-5476.

1369 Wallden, M., Fange, D., Lundius, E.G., Baltekin, O., and Elf, J. (2016). The synchronization of replication
1370   and division cycles in individual *E. coli* cells. Cell *166*, 729-739.

1371 Wang, X., Brandao, H.B., Le, T.B., Laub, M.T., and Rudner, D.Z. (2017). Bacillus subtilis SMC complexes
1372   juxtapose chromosome arms as they travel from origin to terminus. Science *355*, 524-527.

1373 Wang, X., Le, T.B., Lajoie, B.R., Dekker, J., Laub, M.T., and Rudner, D.Z. (2015). Condensin promotes the
1374   juxtaposition of DNA flanking its loading site in Bacillus subtilis. Genes Dev. *29*, 1661-1675.

1375 Wang, Y., Penkul, P., and Milstein, J.N. (2016). Quantitative localization microscopy reveals a novel
1376   organization of a high-copy number plasmid. Biophys. J. *111*, 467-479.

1377 Wegner, A.S., Wintraecken, K., Spurio, R., Woldringh, C.L., de Vries, R., and Odijk, T. (2016).
1378   Compaction of isolated *Escherichia coli* nucleoids: polymer and H-NS protein synergetics. J. Struct.
1379   Biol. *194*, 129-137.

1380 Winkler, H. (2007). 3D reconstruction and processing of volumetric data in cryo-electron
1381   tomography. J. Struct. Biol. *157*, 126-137.

1382 Winkler, H., Zhu, P., Liu, J., Ye, F., Roux, K.H., and Taylor, K.A. (2009). Tomographic subvolume
1383   alignment and subvolume classification applied to myosin V and SIV envelope spikes. J. Struct.
1384   Biol. *165*, 64-77.

1385 Winkler, J., Seybert, A., König, L., Pruggnaller, S., Haselmann, U., Sourjik, V., Weiss, M., Frangakis, A.S.,
1386   Mogk, A., and Bukau, B. (2010). Quantitative and spatio-temporal features of protein aggregation
1387   in *Escherichia coli* and consequences on protein quality control and cellular ageing. EMBO J. *29*,
1388   910-923.

1389 Wong, I.Y., Gardel, M.L., Reichman, D.R., Weeks, E.R., Valentine, M.T., Bausch, A.R., and Weitz, D.A.
1390   (2004). Anomalous diffusion probes microstructure dynamics of entangled F-actin networks.
1391   Phys. Rev. Lett. *92*, 178101.

1392 Wu, F., Swain, P., Kuijpers, L., Zheng, X., Felter, K., Guurink, M., Solari, J., Jun, S., Shimizu, T.S.,
1393   Chaudhuri, D*., et al.* (2019). Cell boundary confinement sets the size and position of the *E. coli*
1394   chromosome. Curr Biol. *29*, 2131-2144.e4

1395 Yang, D., Mannik, J., Retterer, S.T., and Mannik, J. (2020). The effects of polydisperse crowders on the
1396   compaction of the *Escherichia coli* nucleoid. Mol. Microbiol. *113*, 1022-1037

1397 Yang, S., Kim, S., Kim, D.K., Jeon An, H., Bae Son, J., Heden Gynna, A., and Ki Lee, N. (2019).
1398   Transcription and translation contribute to gene locus relocation to the nucleoid periphery in *E.*
1399   *coli*. Nat. Commun. *10*, 5131.

1400 Yonemura, K., and Maeda, H. (1982). A new assay method for DNase by fluorescence polarization and
1401   fluorescence intensity using DNA-ethidium bromide complex as a sensitive substrate. J. Biochem.
1402   *92*, 1297-1303.

1403 Yoshikawa, K., Hirota, S., Makita, N., and Yoshikawa, Y. (2010). Compaction of DNA induced by like-
1404   charge protein: opposite salt-effect against the polymer-salt-induced condensation with neutral
1405   polymer. J. Phys. Chem. Lett. *1*, 1763-1766.

1406 Zhang, C., Shao, P.G., van Kan, J.A., and van der Maarel, J.R. (2009). Macromolecular crowding induced
1407   elongation and compaction of single DNA molecules confined in a nanochannel. Proc. Natl. Acad.
1408   Sci. USA *106*, 16651-16656.

1409 Zhang, K. (2016). Gctf: Real-time CTF determination and correction. J. Struct. Biol. *193*, 1-12.

1410 Zhao, X., Zhang, K., Boquoi, T., Hu, B., Motaleb, M.A., Miller, K.A., James, M.E., Charon, N.W., Manson,
1411   M.D., Norris, S.J*., et al.* (2013). Cryoelectron tomography reveals the sequential assembly of
1412   bacterial flagella in Borrelia burgdorferi. Proc. Natl. Acad. Sci. USA *110*, 14390-14395.

1413 Zheng, S.Q., Palovcak, E., Armache, J.P., Verba, K.A., Cheng, Y., and Agard, D.A. (2017). MotionCor2:
1414   anisotropic correction of beam-induced motion for improved cryo-electron microscopy. Nat.
1415   Methods. *14*, 331-332.

1416 Zhu, J., Penczek, P.A., Schroder, R., and Frank, J. (1997). Three-dimensional reconstruction with
1417   contrast transfer function correction from energy-filtered cryoelectron micrographs: procedure
1418   and application to the 70S *Escherichia coli* ribosome. J. Struct. Biol. *118*, 197-219.

42

1419 Zimm, B.H., and Stockmayer, W.H. (1949). The dimensions of chain molecules containing branches
1420   and rings. J. Chem. Phys. *17*, 1301-1314.

1421 Zimmerman, S.B. (1993). Macromolecular crowding effects on macromolecular interactions: some
1422   implications for genome structure and function. Biochim. Biophys. Acta. *1216*, 175-185.

1423 Zimmerman, S.B. (2002). Toroidal nucleoids in *Escherichia coli* exposed to chloramphenicol. J. Struct.
1424   Biol. *138*, 199-206.

1425 Zimmerman, S.B., and Minton, A.P. (1993). Macromolecular crowding: biochemical, biophysical, and
1426   physiological consequences. Annu. Rev. Biophys. Biomol. Struct. *22*, 27-65.
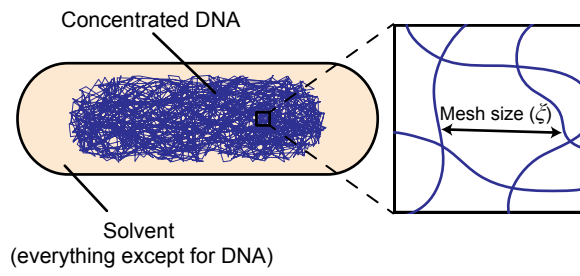
Figure 1
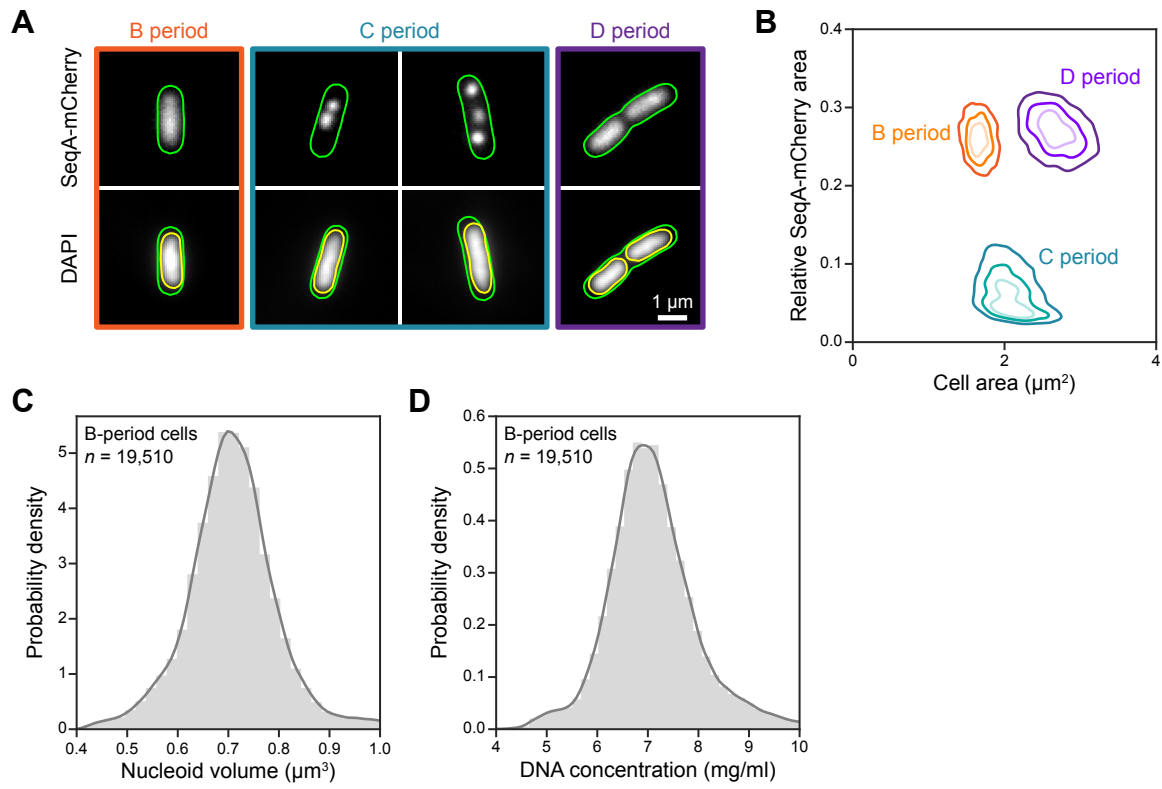
Figure 2
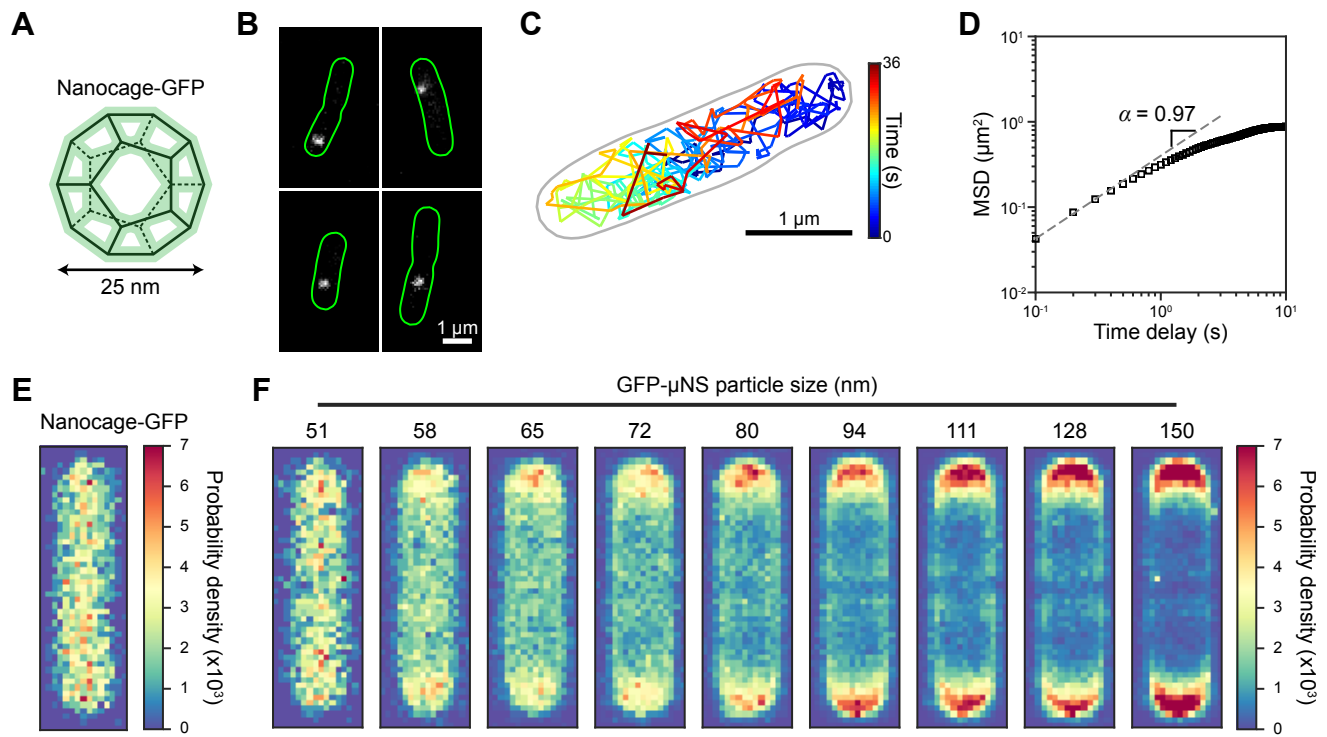
Figure 3
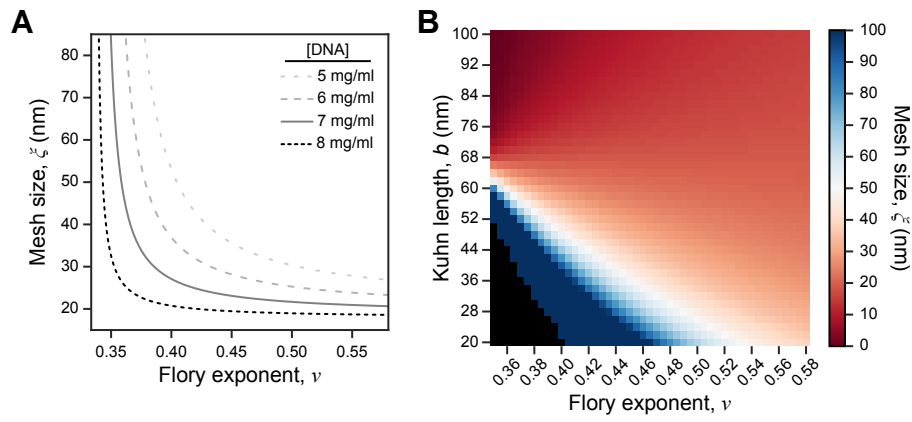
Figure 4
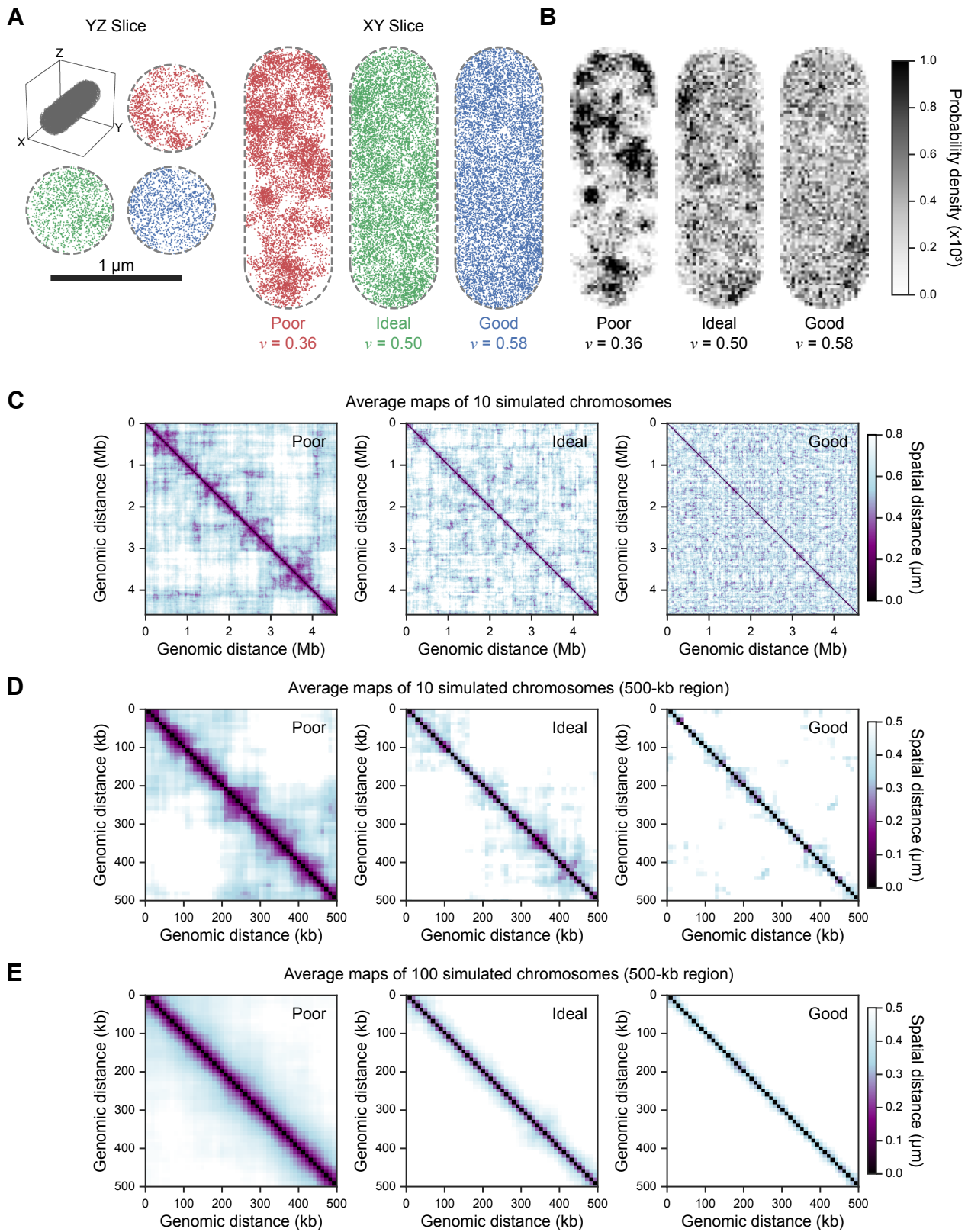
Figure 5
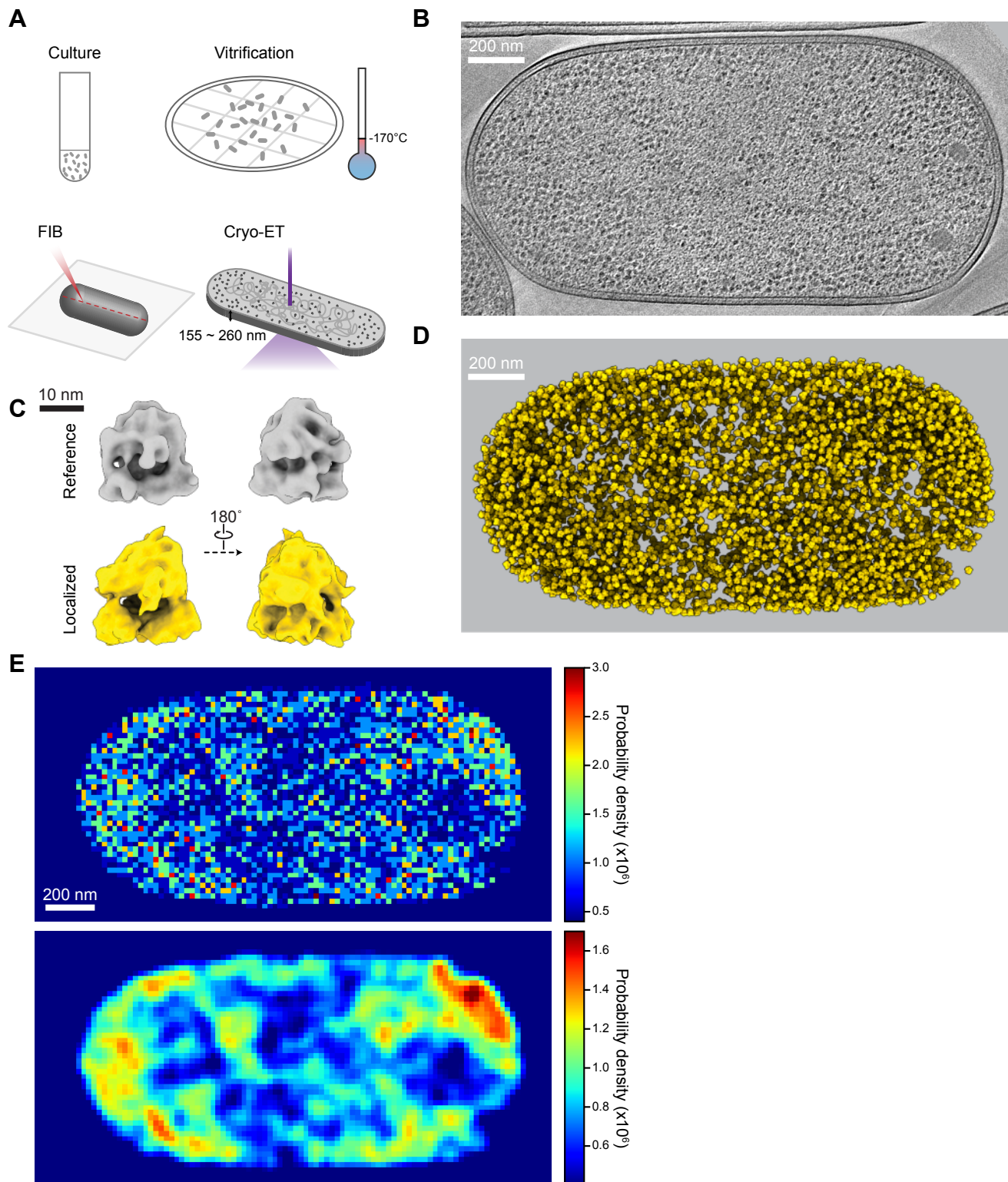
Figure 6
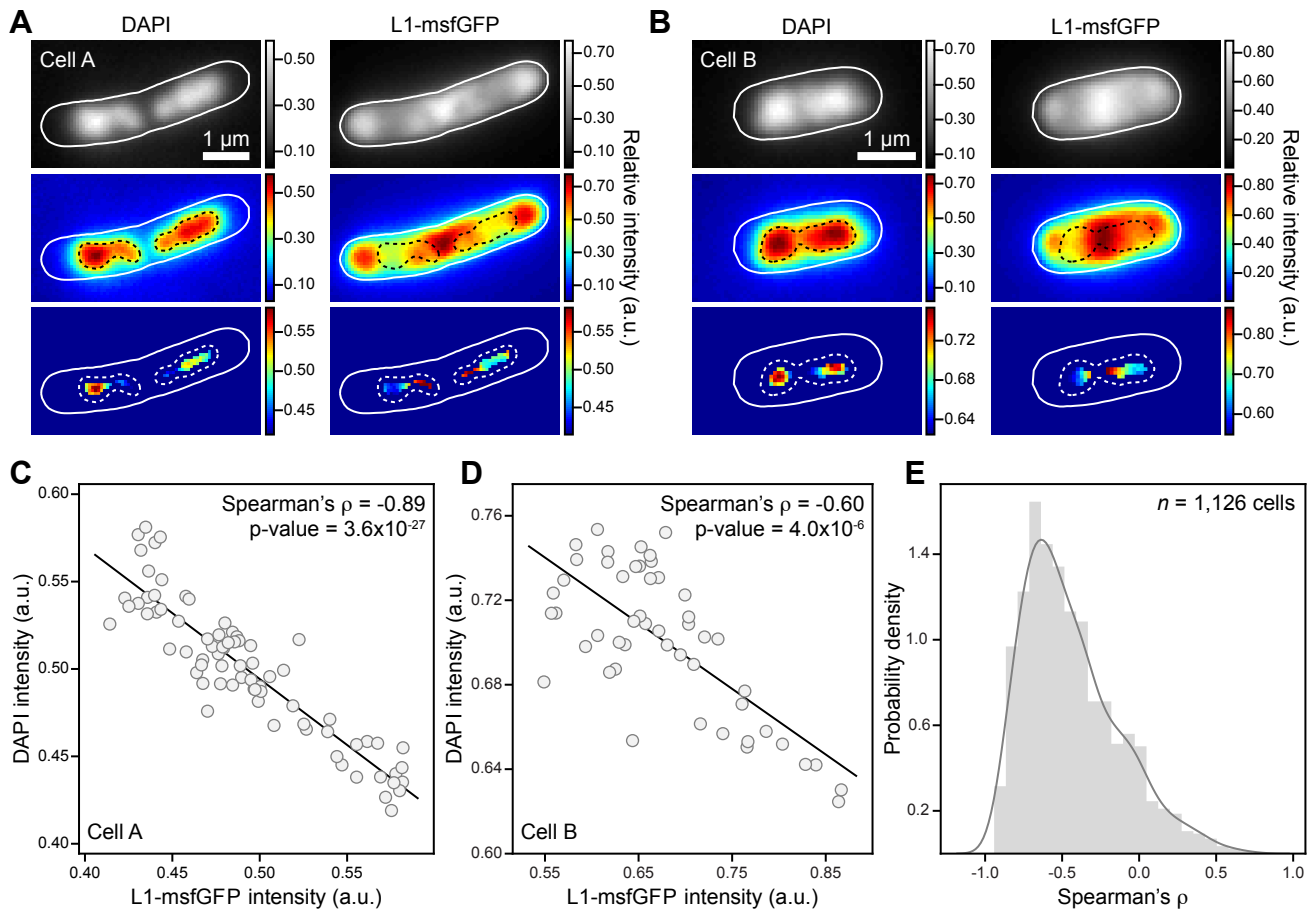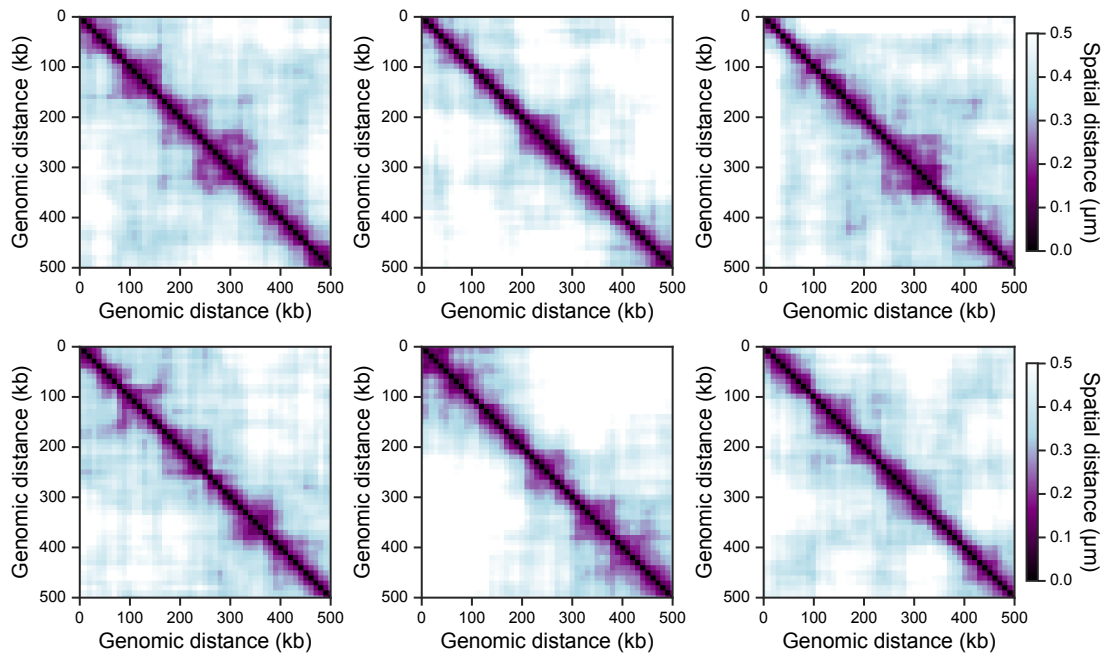
Figure 7
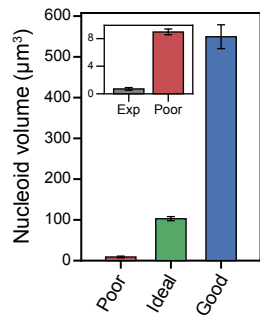
Figure 8
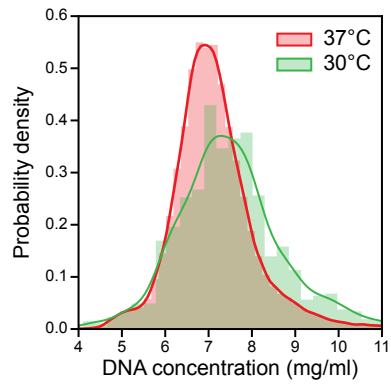
Figure S1
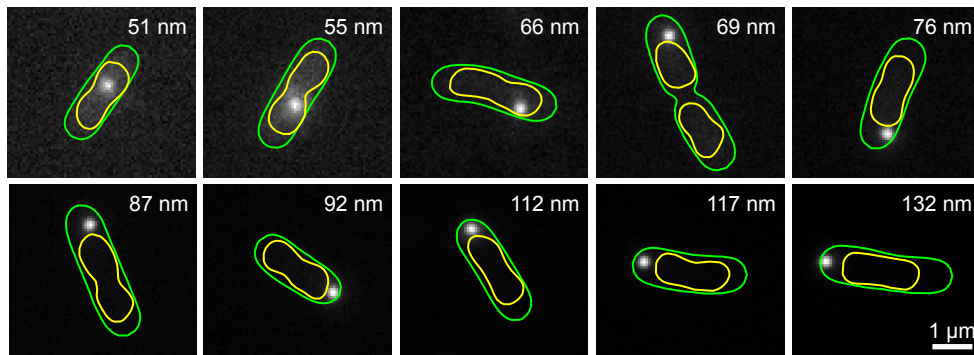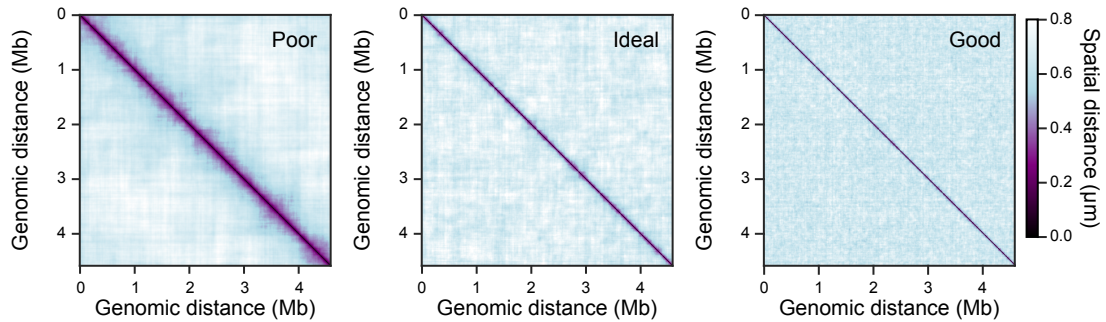
Figure S2

A

6 examples of average maps of 10 simulated chromosomes (500-kb region) in a poor solvent

B
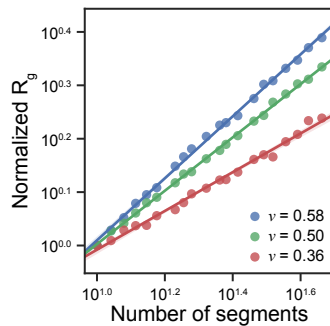

Average maps of 100 simulated chromosomes
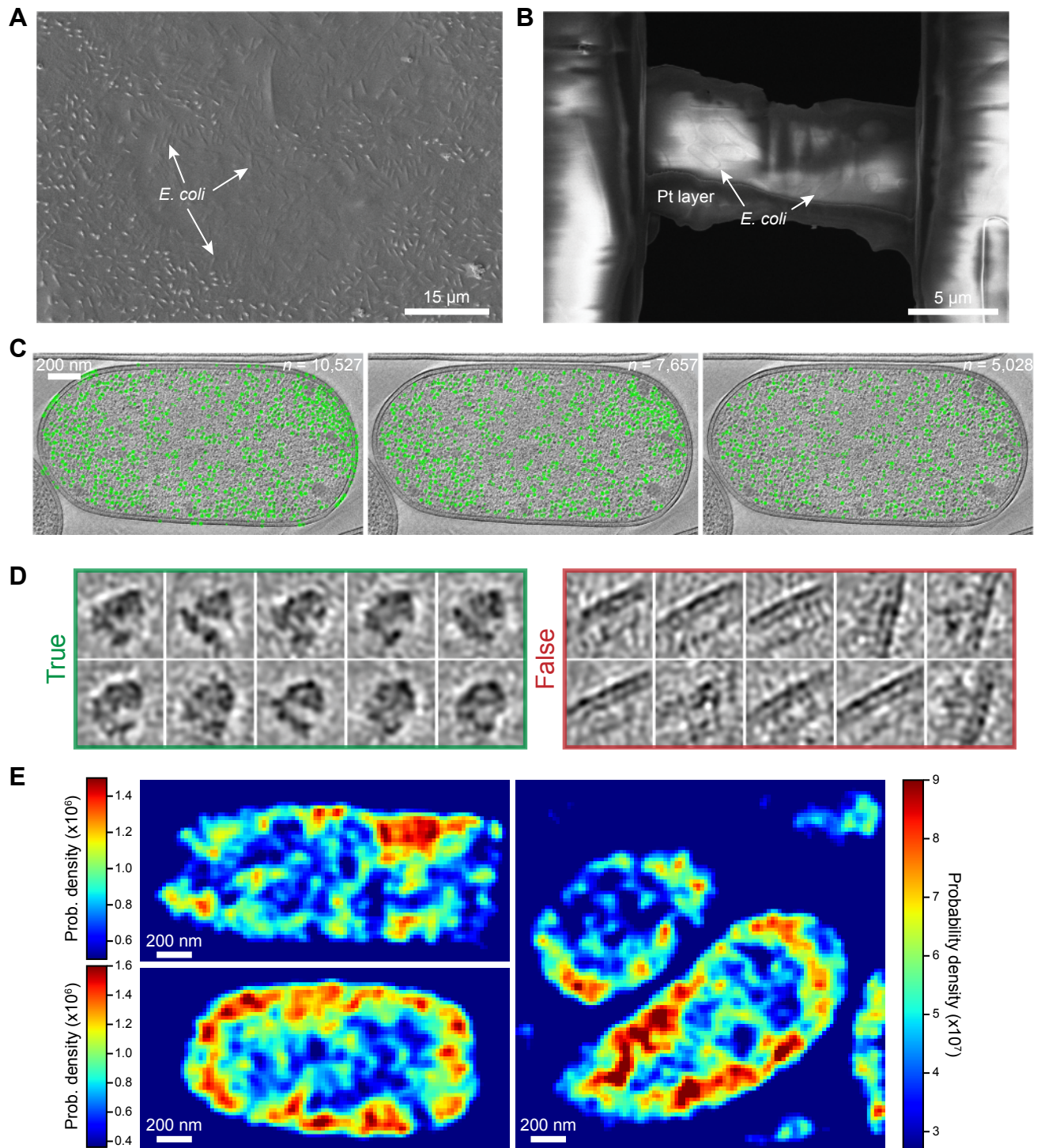
C

Figure S3

Figure S4